Research Square

Preprints are preliminary reports that have not undergone peer review.
They should not be considered conclusive, used to inform clinical practice,
or referenced by the media as validated information.

Nitrate prevents hypoxia-induced bone loss by restraining the gut Prevotella denticola–glutamine–ASCT2–α-ketoglutarate osteoclastogenic axis

Jian Zhou

zhoujian@ccmu.edu.cn

Beijing Laboratory of Oral Health

Zixiao Li

Capital Medical University

Yifan Xu

Beijing Laboratory of Oral Health and Beijing Stomatological Hospital, Capital Medical University, Beijing 100050, China

Zha Xu

Capital Medical University

Chenchen Zhou

State Key Laboratory of Oral Diseases and National Clinical Research Center for Oral Diseases, West China Hospital of Stomatology, Sichuan University https://orcid.org/0000-0002-6427-5869

Xiaoyu Li

Capital Medical University

Haoran Du

Anhui Medical University

Kang Gao

Capital Medical University

Yibo Liu

Capital Medical University

Zhaoyao Qi

Capital Medical University

Xiaochen Fang

Capital Medical University

Weihua Guo

Kunming Medical University

Xicheng Liu

Capital Medical University

Songlin Wang

Capital Medical University https://orcid.org/0000-0002-7066-2654

Article

Keywords:

Posted Date: November 25th, 2026

DOI: https://doi.org/10.21203/rs.3.rs-11518987/v1

License: This work is licensed under a Creative Commons Attribution 4.0 International License.
Read Full License

Additional Declarations: There is no conflict of interest

Nitrate prevents hypoxia-induced bone loss by restraining the gut *Prevotella denticola*–glutamine–ASCT2–α-ketoglutarate osteoclastogenic axis

Zixiao Li[1,2,3] Yifan Xu[1,2,4] Xu Zha[2,5] Chenchen Zhou[6] Xiaoyu Li[1] Haoran Du[1,7] Kang Gao[8] Yibo Liu[2,5] Zhaoyao Qi[2,5] Xiaochen Fang[1,2,3] Weihua Guo[9] Xicheng Liu[2,5] Songlin Wang[1,10,11] Jian Zhou[1,2,3]

1. Laboratory of Oral Health and Homeostatic Medicine, Beijing Stomatological Hospital and Beijing Laboratory of Oral Health, Capital Medical University, Beijing, China
2. Laboratory for Clinical Medicine, Capital Medical University, Beijing, China
3. International Medical Services and Healthcare center, Beijing Stomatological Hospital, Capital Medical University, Beijing, China
4. Department of Oral Implantology, Beijing Stomatological Hospital, Capital Medical University, Beijing, China
5. Department of Physiology and Pathophysiology, School of Basic Medical Sciences, Capital Medical University, Beijing, China
6. State Key Laboratory of Oral Diseases & National Clinical Research Centre for Oral Diseases & Department of Pediatric Dentistry, West China Hospital of Stomatology, Sichuan University, Chengdu, China
7. Department of Orthodontics, College & Hospital of Stomatology, Anhui Medical University, Anhui Provincial Key Laboratory of Oral Diseases Research, Hefei 230032, China.
8. Department of Oral and Maxillofacial Surgery Clinic, Beijing Stomatological Hospital, Capital Medical University, Beijing, China
9. Yunnan Key Laboratory of Stomatology & Department of Pediatric Dentistry, The Affiliated Stomatology Hospital, Kunming Medical University, Kunming, China
10. Laboratory of Oral Homeostatic Medicine, School of Medicine and SUSTech Homeostatic Medicine Institute (SHMI), Southern University of Science and Technology, Shenzhen, China
11. Department of Biochemistry and Molecular Biology, Capital Medical University School of Basic Medicine, Beijing, China

Corresponding author: Prof. Jian Zhou
Prof. Jian Zhou
Email: zhoujian@ccmu.edu.cn
Capital Medical University School of Stomatology, No. 9 Fanjia Village Road, 100070, Beijing , China

Abstract

Chronic hypoxia causes progressive bone loss, but its mechanisms remain unclear and effective interventions are limited. Given its potential to regulate bone and gut homeostasis, we investigated whether inorganic nitrate protects against hypoxia-induced bone loss. In mice exposed to 10% O_2 for 3 months, nitrate preserved trabecular microarchitecture, improved bone formation and reduced osteoclast-associated bone resorption. Fecal microbiota transplantation from nitrate-treated donors improved bone phenotypes in hypoxic recipients, supporting a transferable gut-associated component of protection. Metagenomic and metabolomic analyses identified hypoxia-induced enrichment of *Prevotella denticola* and glutamine-related metabolic abnormalities, both attenuated by nitrate. *P. denticola* supplementation aggravated hypoxic bone loss and increased serum glutamine. Nitrite, a downstream metabolite of nitrate, inhibited *P. denticola* growth, reduced glutamine synthetase activity and decreased extracellular glutamine in vitro. To examine the functional relevance of these metabolic changes, we assessed glutamine supplementation and transport. Glutamine supplementation exacerbated hypoxic bone loss, while hypoxia increased ASCT2 expression and intracellular glutamine accumulation during osteoclast differentiation. Pharmacological transport inhibition and deficiency of the ASCT2-encoding gene *Slc1a5* suppressed osteoclastogenesis; *Slc1a5*-deficient mice retained more trabecular bone under hypoxia. [U-$^{13}C_5$]glutamine tracing and rescue experiments implicated α-ketoglutarate (α-KG) as a downstream mediator of ASCT2-associated glutamine metabolism. α-KG restored osteoclastogenesis in *Slc1a5*-deficient cells and reduced H3K27me3 enrichment at the *Nfatc1* transcription start site, supporting an epigenetic link. These findings implicate a *P. denticola*-associated glutamine–ASCT2–α-KG pathway in hypoxic bone loss. They suggest that nitrate may preserve gut–bone homeostasis by modulating microbial and metabolic changes under chronic hypoxia.

Introduction

Chronic hypoxia is widespread in high-altitude regions and poses an ongoing public health challenge. On the basis of population and geospatial data from 2019, approximately 14.4 million people worldwide lived at elevations of ≥3,500 m, with China having the largest population above this threshold.[1] After ascending to high altitude, individuals who are not adequately acclimatized may develop acute mountain sickness, with symptoms such as headache, dizziness, fatigue, and nausea.[2] Beyond acute altitude illness, prolonged hypoxic exposure may affect multiple organ systems, with bone as a potential target tissue. Bone loss and deterioration of bone microarchitecture have been observed in animal models of chronic hypoxia.[3] Elucidating the mechanisms underlying hypoxia-induced bone loss and identifying interventions that improve bone and metabolic homeostasis are therefore important for maintaining long-term skeletal health in high-altitude populations.[4]

The mechanisms through which hypoxia disrupts bone homeostasis remain incompletely understood. Previous studies have shown that chronic hypoxia inhibits osteoblast proliferation, differentiation, and mineralization while promoting osteoclast formation and bone resorption.[5,6] Hypoxia-inducible factors (HIFs) mediate oxygen sensing in bone cells, and HIF-1α can promote osteoclast activation and bone loss in estrogen-deficiency models.[7] These studies have revealed local mechanisms through which hypoxia directly affects bone cells.[8] Bone homeostasis is also regulated by systemic metabolic status, inflammatory responses, and interorgan signals. How systemic physiological changes induced by chronic hypoxia contribute to dysregulated bone remodeling therefore remains unclear.

The gut microbiota is an important interorgan regulatory system that links systemic physiology to bone homeostasis. In sex steroid-deficient mice, increased intestinal permeability is accompanied by increased levels of pro-osteoclastogenic cytokines in the gut and bone marrow. These responses are absent in germ-free mice, providing causal evidence that the gut microbiota contributes to bone damage.[9,10] The gut microbiota may also play a protective role in maintaining bone homeostasis. Microbially derived butyrate promotes WNT10B expression in $CD8^+$ T cells through a regulatory T-cell-dependent mechanism, thereby enhancing bone formation.[11] Together, these findings indicate that the gut microbiota can influence remodeling in distant bone tissue through immune regulation and microbial metabolism.[12] Recent work has further associated changes in the gut microbiota during chronic hypoxia with attenuated bone damage. However, the key microorganisms involved and the pathways through which they affect bone cells remain unclear.[3]

Microbial metabolites contribute to the gut microbiota-mediated regulation of bone remodeling by modulating bone cell metabolism and signaling. Among these, the short-chain fatty acids butyrate and propionate alter osteoclast energy metabolism, suppress osteoclast differentiation, and attenuate experimental bone loss.[13] Microbial amino acid metabolism also generates

bioactive molecules that influence bone cell function. For example, microbial degradation of histidine produces imidazole propionate, which can modulate host mTORC1 signaling. Subsequent studies have shown that this metabolite inhibits osteoblast differentiation through the p38γ–AMPK pathway and induces bone loss in mice.[14,15] Amino acids produced by the gut microbiota and their subsequent conversion within the host also contribute to skeletal regulation. For example, the microbial production of L-citrulline and its conversion to L-arginine regulate bone adaptation to mechanical loading. L-arginine enhances this process by activating a nitric oxide–calcium positive feedback loop in osteocytes. These findings suggest that microbiota-associated amino acid supply and metabolism provide important links between the gut environment and bone cell function. However, whether the gut microbiota alters amino acid substrate availability to influence bone cell metabolism and remodeling during chronic hypoxia remains unclear.

Glutamine metabolism links amino acid biosynthesis to energy metabolism and plays important roles in regulating bone cell function and bone homeostasis. Previous studies have shown that glutaminolysis supplies the precursors required for nucleotide and amino acid synthesis during osteoclast differentiation. Inhibiting this process attenuated ovariectomy-induced bone loss in mice.[16,17] Glutamine can also be converted through glutamate to α-ketoglutarate (α-KG), which is involved in mitochondrial metabolism. This metabolic route can regulate osteoclast differentiation by altering histone methylation.[18] These findings indicate that glutamine utilization links the metabolic demands of bone cells to the regulation of their differentiation.[19,20] However, the role of glutamine metabolism in chronic hypoxia-induced disruption of bone homeostasis remains unclear. Specifically, whether the gut microbiota alters glutamine availability to regulate its uptake and downstream metabolism in osteoclasts, thereby influencing bone remodeling, remains unknown.

Current pharmacological therapies for osteoporosis reduce fracture risk primarily by inhibiting bone resorption or promoting bone formation, and their efficacy has been supported by clinical trials.[21] However, maintaining these therapeutic benefits over the long term remains challenging. Discontinuation of denosumab, for example, can lead to rebound bone turnover and decreased bone mineral density, with multiple vertebral fractures occurring in some patients.[22] These limitations indicate that osteoporosis management should address bone mineral density and fracture risk during treatment, as well as the maintenance of bone homeostasis during long-term therapy and after treatment discontinuation. With respect to chronic hypoxia-induced bone loss, interventions targeting bone tissue alone may not address pathological factors outside the skeleton. Because the gut microbiota and its metabolic activity can influence bone cell function, correcting hypoxia-associated gut abnormalities may offer a new approach to improving bone homeostasis. Identifying interventions that modulate the gut environment, maintain metabolic homeostasis, and improve the bone phenotype is therefore of considerable research interest.

Inorganic nitrate contributes to systemic homeostasis by regulating vascular function, glucose and lipid metabolism, and mitochondrial energy utilization.[23,24] Clinical studies have shown that dietary nitrate supplementation decreases blood pressure in patients with hypertension and improves mitochondrial oxidative phosphorylation efficiency in human skeletal muscle.[25,26] Animal studies have further shown that nitrate ameliorates impaired glucose metabolism and reduces visceral fat accumulation and circulating triglyceride levels in endothelial nitric oxide synthase-deficient mice.[27] In bone, nitrate supplementation promotes bone marrow mesenchymal stem cell proliferation and osteogenic differentiation and attenuates bone loss in ovariectomized mice. These osteogenic effects are associated with the activation of EGFR/AKT/ERK and mTOR/S6K signaling.[28] A recent study further revealed that dietary nitrate supplementation restored Sialin expression in aged mice. Sialin recruits STAT3 phosphorylated at Ser727 to mitochondria, maintaining mitochondrial bioenergetic function in mesenchymal stem cells, promoting osteogenic differentiation, and improving bone homeostasis. In the gut, nitrate ameliorates experimental colitis by modulating microbiota homeostasis.[29] The protective effects of nitrate on tissue homeostasis also extend to hypoxic conditions. For example, in hypoxic mice, nitrate activates EGFR/PI3K/AKT/mTOR signaling, promoting HIF-1α nuclear translocation and HIF-1α-mediated transcription of tight junction proteins. This response preserves intestinal epithelial barrier integrity and alleviates intestinal injury.[30] The effects of nitrate on bone cell metabolism and its intestinal protective effects under hypoxia suggest potential benefits against hypoxia-induced bone loss. However, whether these effects confer skeletal protection during chronic hypoxia, and whether the gut microbiota and associated metabolic changes contribute to this protection, require direct experimental evidence.

In this study, we investigated how the gut microbiota and associated metabolic changes influence bone remodeling under chronic hypoxia, and whether nitrate modulates these processes to attenuate bone loss. Using a chronic hypoxia model, we combined gut microbiota metagenomic sequencing, metabolomics, fecal microbiota transplantation (FMT), and bacterial supplementation to assess the contribution of the microbiota to nitrate-mediated bone protection. We subsequently used metabolic interventions, isotope tracing, and epigenetic analyses to investigate how microbiota-associated changes affect glutamine uptake, glutamine–α-ketoglutarate (Gln–α-KG) metabolism, and osteoclast differentiation. Together, these approaches aimed to identify the metabolic pathway linking the gut microbiota to bone remodeling and clarify how nitrate regulates gut–bone homeostasis under chronic hypoxia.

Results

1. Nitrate supplementation alleviates hypoxia-induced bone loss in mice.

To define an exposure duration for studying chronic hypoxia-induced bone loss, we compared femoral trabecular microarchitecture in mice exposed to 10% O_2 for 1 or 3 months. Microcomputed tomography (micro-CT) revealed lower bone volume fraction (BV/TV), bone surface-to-tissue volume ratio (BS/TV) and trabecular number (Tb.N), together with greater trabecular separation (Tb.Sp), after 3 months than after 1 month of hypoxia (Supplementary Fig. 1). These findings supported the use of a 3-month hypoxia exposure for the intervention experiments.

We then assessed the effects of nitrate supplementation using C57BL/6J mice maintained under normoxia (21% O_2), hypoxia (10% O_2), or hypoxia with nitrate supplementation for 3 months (Fig. 1a). Compared with normoxic control mice, hypoxia-exposed mice had lower body weights during the intervention period (Fig. 1b).

Micro-CT revealed that hypoxia reduced femoral trabecular bone mass and impaired bone microarchitecture. These changes were reflected by decreased bone mineral density (BMD), BV/TV, BS/TV and Tb.N (Fig. 1c–g). Compared with hypoxia alone, nitrate supplementation increased each of these parameters (Fig. 1c–g). Hematoxylin and eosin (H&E) and Masson's trichrome staining further revealed reduced trabecular bone and collagen-rich bone matrix in hypoxic mice, and these changes were attenuated by nitrate supplementation (Fig. 1i, j, l). Tartrate-resistant acid phosphatase (Trap) staining revealed that hypoxia increased the proportion of bone surface covered by osteoclasts (Oc.S/BS), whereas nitrate supplementation reduced this proportion (Fig. 1k, m).

Serum bone turnover markers showed corresponding changes. Hypoxia decreased serum osteocalcin (OCN) concentrations and increased C-terminal telopeptide of type I collagen (CTX-1) concentrations, whereas nitrate supplementation attenuated both changes (Fig. 1n, o). Compared with hypoxia alone, Calcein labeling showed that nitrate supplementation increased the mineral apposition rate (MAR) and bone formation rate per bone surface (BFR/BS) (Fig. 1h, p, q). Together, these findings support a protective effect of nitrate supplementation against hypoxia-induced bone loss, accompanied by improved indices of bone formation and reduced indices of bone resorption.

2. The gut microbiota from nitrate-treated donors protects against hypoxia-induced bone loss

To assess whether the gut microbiota contributes to the skeletal effects of nitrate supplementation, mice were treated with broad-spectrum antibiotics to deplete the intestinal microbiota. Compared with controls, antibiotic-treated mice showed markedly reduced

bacterial growth in fecal cultures, together with lower observed species richness and Shannon diversity (Fig. 2a–c). Principal coordinate analysis (PCoA) based on unweighted UniFrac distances showed clear separation between the control and antibiotic-treated groups, indicating altered microbial community composition (Fig. 2d).

We next performed fecal microbiota transplantation (FMT) in hypoxia-exposed mice. FMT-H recipients received fecal material from hypoxia-exposed donors, whereas FMT-N recipients received fecal material from donors supplemented with nitrate in their drinking water. Body weight trajectories were similar among the hypoxia-exposed groups during the intervention (Fig. 2e). Micro-CT analysis revealed a low-bone-mass phenotype in FMT-H recipients, characterized by reduced femoral BMD, BS/TV, BV/TV, and Tb.N. FMT-N attenuated these skeletal abnormalities, indicating that fecal transplantation from nitrate-treated donors alleviated hypoxia-induced bone loss (Fig. 2f–j).

Histological analyses further supported the skeletal protection conferred by FMT-N. H&E staining revealed disrupted trabecular architecture and reduced bone matrix in hypoxic mice, whereas femoral morphology was better preserved in FMT-N recipients (Fig. 2k). Masson's trichrome staining showed a greater bone matrix area in FMT-N recipients than in hypoxic mice (Fig. 2m, n). Hypoxia increased serum CTX-1 concentrations and the proportion of bone surface covered by osteoclasts (Oc.S/BS), whereas FMT-N reduced both measures (Fig. 2l, p). Together, these findings revealed that fecal transplantation from nitrate-treated donors attenuated hypoxia-induced bone loss in recipient mice, supporting the contribution of the gut microbiota to nitrate-mediated bone protection.

3. Nitrate supplementation reshapes the gut microbiota and alleviates *Prevotella denticola*-associated bone loss in hypoxic mice

To characterize the effects of nitrate supplementation on the gut microbiota during hypoxia, we performed fecal metagenomic sequencing in control, hypoxia, and hypoxia+Nit mice. Compared with the control conditions, hypoxia increased both microbial richness and diversity, as measured by the Chao1 estimator and the Shannon index. Neither index differed significantly between the hypoxia and hypoxia+Nit groups (Fig. 3a, b). In contrast, principal coordinate analysis (PCoA) based on Bray–Curtis distances revealed distinct clustering among the three groups, indicating differences in overall microbial community composition (Fig. 3c). Taxonomic analyses further revealed marked differences in the distribution and relative abundance of bacterial taxa across the groups (Fig. 3d–f). Compared with hypoxia alone, nitrate supplementation also increased the Firmicutes-to-Bacteroidetes ratio (Fig. 3h).

Linear discriminant analysis effect size (LEfSe) revealed several species that were differentially enriched among the groups, including enrichment of *P. denticola* under hypoxia (Fig. 3g). Metagenomic quantification confirmed that the relative abundances of *P. denticola*, *Prevotella*

sp. Rep29, *Prevotella dentalis*, and *Prevotella intermedia* increased in hypoxic mice but decreased following nitrate supplementation (Fig. 3i–l). These findings revealed that *P. denticola* is a nitrate-responsive taxon potentially associated with hypoxia-induced skeletal deterioration.

To assess the functional relevance of *P. denticola*, hypoxia-exposed mice were supplemented with the bacterium, either alone or together with nitrate. Representative CT and Masson's trichrome-stained images indicated that *P. denticola* supplementation aggravated the loss of trabecular bone and bone matrix under hypoxia, whereas nitrate cosupplementation attenuated these changes (Fig. 3m, n). Consistent with these findings, Trap staining and histomorphometric analysis revealed that *P. denticola* increased osteoclast surface per bone surface (Oc.S/BS), whereas nitrate cosupplementation markedly reduced this increase (Fig. 3o,p). Together, these findings indicate that nitrate supplementation reshaped the hypoxia-associated gut microbiota, reduced the relative abundance of *P. denticola*, and attenuated the skeletal alterations associated with supplementation with this bacterium.

4. Nitrate supplementation modulates hypoxia-associated metabolic alterations and amino acid profiles in mice supplemented with *P. denticola*

To characterize metabolic changes following nitrate supplementation, we performed untargeted fecal metabolomic profiling in control, hypoxia, and hypoxia+Nit mice. Partial least-squares discriminant analysis (PLS-DA) separated the three groups, and pairwise comparisons revealed changes in the abundance of multiple fecal metabolites (Fig. 4a–c). The tetrapeptide Thr–Ala–Gln–Glu was more abundant under hypoxia than under control conditions and decreased following nitrate supplementation, a pattern also shown in the heatmap of differentially abundant metabolites (Fig. 4d, e). Pathway enrichment analysis highlighted alanine, aspartate and glutamate metabolism, as well as D-amino acid metabolism (Fig. 4f).

We next analyzed serum amino acid profiles. The serum glutamine concentration was higher in hypoxic mice than in control mice and lower following nitrate supplementation than under hypoxia alone (Fig. 4g, h). Compared with hypoxia alone, nitrate supplementation also reduced the combined sarcosine, alanine and β-alanine signal and the concentrations of lysine, asparagine and aspartate (Fig. 4j–m). Serum glutamate concentration did not significantly differ among the three groups (Fig. 4i).

To determine the relationships between these metabolic changes and gut bacteria, we examined associations between bacterial abundance and metabolite levels. The correlation matrix revealed a positive associationcorrelation between *P. denticola* abundance and fecal Thr–Ala–Gln–Glu levels (Fig. 4n). Across 15 mice, *P. denticola* abundance was positively correlated with the fecal Thr–Ala–Gln–Glu levels (Pearson r = 0.95) and serum glutamine concentration (Pearson r = 0.52; Fig. 4o, p). In the bacterial supplementation experiment, the serum glutamine

concentration was higher in mice given *P. denticola* than in mice exposed to hypoxia alone. Compared with *P. denticola* supplementation alone, nitrate cosupplementation reduced serum glutamine concentrations (Fig. 4q). The combined sarcosine, alanine and β-alanine signal did not differ significantly among these groups, whereas serum aspartate concentration was higher with nitrate cosupplementation than with *P. denticola* alone (Fig. 4r, s). Together, these results show that nitrate supplementation was accompanied by changes in the fecal and serum metabolic profiles under hypoxia and attenuated the increase in the level of serum glutamine following *P. denticola* supplementation.

5. Nitrite alters extracellular amino acid metabolism and suppresses *Prevotella denticola* growth

To determine whether nitrate itself or its reduction product, nitrite, directly affects *P. denticola*, we first screened their effects on bacterial growth across different concentrations (Supplementary Fig. 2). At 48 h, OD_{600} did not differ significantly from the untreated control at 0.5 or 1 mM nitrate but was lower at 2, 10 and 100 mM nitrate. In contrast, nitrite reduced OD_{600} at every tested concentration from 0.5 to 10 mM. Based on these screening results, we selected nitrite for further investigation and used 2 mM nitrite for 24 h in the subsequent metabolic assays.

Under these conditions, nitrite reduced *glnA* and *glnB* expression and glutamine synthetase activity compared with untreated cultures (Fig. 5a–c). Targeted amino acid profiling of culture supernatants separated control and nitrite-treated samples in principal component analysis, while the volcano plot and heatmap revealed differences in extracellular amino acid abundance (Fig. 5d – f). Pathway enrichment and metabolite – pathway mapping highlighted alanine, aspartate and glutamate metabolism, D-amino acid metabolism, and amino acid biosynthesis (Fig. 5g, h). Compared with the control, nitrite-treated supernatants contained lower concentrations of L-glutamic acid, L-glutamine, L-asparagine, β-alanine and L-tyrosine, but a higher concentration of L-serine (Fig. 5i–n).

We further examined bacterial growth, biofilm formation and morphology across the tested nitrite concentrations. Agar plate images and crystal violet staining showed reduced bacterial growth and biofilm staining after nitrite treatment (Fig. 5o, p). Scanning electron microscopy revealed changes in bacterial morphology, and live/dead staining showed increased red fluorescence at higher nitrite concentrations (Fig. 5q, r). Together, these results show that nitrite suppresses *P. denticola* growth and is accompanied by reduced glutamine synthesis-related measures and altered extracellular amino acid abundance, including lower L-glutamine concentrations.

6. Glutamine aggravates hypoxia-induced bone loss and promotes glutamine uptake-dependent osteoclastogenesis

To determine whether glutamine contributes to hypoxia-induced skeletal damage, C57BL/6J mice were exposed to hypoxia (10% O_2) with or without glutamine supplementation for 3 months. Microcomputed tomography (micro-CT) analysis revealed that compared with hypoxia alone, glutamine supplementation further reduced the femoral bone mineral density (BMD), bone surface-to-tissue volume ratio (BS/TV), bone volume fraction (BV/TV), and trabecular number (Tb.N) (Fig. 6a, d–g). Masson's trichrome staining revealed a reduction in bone matrix, whereas Trap staining and histomorphometric analysis revealed an increase in osteoclast surface area per bone surface (Oc. S/BS) (Fig. 6b, c, h). These results indicate that glutamine supplementation aggravated bone loss under hypoxia, accompanied by increases in osteoclast-related measures.

To test whether hypoxia alters glutamine uptake during osteoclast differentiation, we isolated primary mouse macrophages and induced their differentiation under normoxic or hypoxic conditions. Glutamine uptake increased over the course of differentiation and was greater under hypoxia on day 7 (Fig. 6i, j). Hypoxia also increased the expression of *Trap, Traf6, Ctsk, Nfatc1*, and the ASCT2-encoding gene *Slc1a5* (Fig. 6k). Immunofluorescence was used to detect ASCT2 and CTSK signals in femoral sections, whereas immunoblotting of osteoclasts differentiated in vitro revealed increased expression of both proteins under hypoxia (Fig. 6l–o). Consistent with these findings, hypoxia increased the number of Trap-positive multinucleated cells during differentiation (Fig. 6p, q). Direct supplementation with 4 mM nitrate did not significantly alter osteoclast numbers, F-actin ring formation, or osteoclast-related gene expression under hypoxia (Supplementary Fig. 3). Together with the preceding microbiota and metabolite findings, this observation is consistent with nitrate exerting part of its skeletal protective effects through indirect modulation of glutamine availability. We therefore next examined the functional contribution of glutamine utilization and downstream metabolism to osteoclast differentiation under hypoxia.

Molecular docking predicted hydrogen-bond interactions between glutamine and residues within an ASCT2 binding pocket (Supplementary Fig. 4).To assess the contribution of glutamine uptake, we treated osteoclasts with the ASCT2 inhibitor V-9302 and observed reduced glutamine uptake (Fig. 6r). Compared with Glutamine supplementation, 1, 2, and 4 mM increased the number of Trap-positive multinucleated cells, with the greatest increase observed at 2 mM. Adding V-9302 in the presence of 2 mM glutamine reduced this number (Fig. 6 s, t). Glutamine supplementation also increased the expression of *Trap, Traf6, Ctsk*, and *Nfatc1*, whereas V-9302 attenuated these increases; NFATc1 protein expression changed accordingly (Fig. 6u, v). Together, these findings support a role for glutamine uptake in hypoxia-associated osteoclast formation and implicate ASCT2-associated transport in this process.

7. ASCT2 deficiency preserves bone mass under hypoxia and impairs glutamine-dependent osteoclastogenesis

To assess the role of ASCT2 in skeletal changes under hypoxia, we compared hypoxia-exposed wild-type (WT) and *Slc1a5*$^{-/-}$ mice. Microcomputed tomography (micro-CT) revealed greater trabecular bone mass in *Slc1a5*$^{-/-}$ mice than in WT mice (Fig. 7a). Bone mineral density (BMD), bone volume fraction (BV/TV), bone surface-to-tissue volume ratio (BS/TV), and trabecular number (Tb.N) were also higher in *Slc1a5*$^{-/-}$ mice (Fig. 7b–e). Together, these results indicate that *Slc1a5*$^{-/-}$ mice had greater trabecular bone mass than WT mice under hypoxia.

We next examined the role of ASCT2 in osteoclast differentiation. Compared with WT cells, *Slc1a5*$^{-/-}$ cells formed markedly fewer Trap-positive multinucleated osteoclasts and F-actin rings (Fig. 7f–h). *Slc1a5* deficiency also reduced the expression of osteoclastogenesis-related genes, including *Trap*, *Traf6*, *Ctsk*, and *Nfatc1* (Fig. 7i). NFATc1 and CTSK protein levels were likewise lower in *Slc1a5*$^{-/-}$ osteoclasts (Fig. 7j–l). These results support a role for ASCT2 in osteoclast differentiation. We also examined osteoblasts differentiated from bone marrow mesenchymal stem cells (BMSCs). Hypoxia reduced osteogenic marker expression and RUNX2 and ALP fluorescence, whereas ASCT2 and GLS expression did not differ significantly from normoxic controls (Supplementary Fig. 5). Together with the osteoclast findings, these results suggest distinct hypoxic responses of glutamine-related proteins in the two cell types and support the involvement of osteoclast glutamine metabolism in hypoxia-associated bone loss.

To trace the metabolic fate of glutamine during osteoclastogenesis, we performed [U-$^{13}C_5$]glutamine tracing. Glutamine-derived carbon was detected in glutamate and α-ketoglutarate (α-KG), while labeling of tricarboxylic acid cycle intermediates was consistent with oxidative metabolism and reductive carboxylation (Fig. 7m–q). These results indicate that glutamine supplies carbon to α-KG and downstream metabolites during osteoclast differentiation. BPTES treatment and silencing of Got2 or Glud1 each reduced α-KG levels and osteoclast differentiation (Supplementary Fig. 6).

We then examined whether α-KG supplementation could compensate for impaired osteoclastogenesis in *Slc1a5*$^{-/-}$ cells. In *Slc1a5*$^{-/-}$ cultures, α-KG supplementation increased osteoclastogenesis-related gene expression and substantially restored the formation of Trap-positive multinucleated cells and F-actin rings (Fig. 7r–u). This result is consistent with α-KG acting as a downstream mediator of ASCT2-associated glutamine metabolism.

Because α-KG is linked to histone demethylation, we examined histone methylation in WT and *Slc1a5*$^{-/-}$ osteoclasts. *Slc1a5* deficiency was accompanied by increased H3K27me3 levels, whereas H3K4me3 and H3K9me3 showed no evident changes (Fig. 7v). Increased H3K27me3 staining was also detected in femoral sections from *Slc1a5*$^{-/-}$ mice (Fig. 7w). Chromatin

immunoprecipitation–quantitative PCR revealed greater H3K27me3 enrichment near the *Nfatc1* transcription start site in *Slc1a5*$^{-/-}$ osteoclasts; α-KG supplementation reduced this enrichment (Fig. 7x). Together, these findings support a role for ASCT2 in osteoclastogenesis and suggest that altered H3K27me3 enrichment at the *Nfatc1* locus may provide an epigenetic link.

Discussion

We found that bone loss during chronic hypoxia was accompanied by enrichment of gut *P. denticola* and increased glutamine uptake by osteoclasts. Supplementation with *P. denticola* exacerbated skeletal damage and was accompanied by increased circulating glutamine levels, whereas inhibition of glutamine uptake or *Slc1a5* deletion reduced osteoclast formation. α-KG supplementation partially restored osteoclast formation in Slc1a5-deficient cells and reduced H3K27me3 enrichment at the Nfatc1 locus. Nitrate supplementation decreased the abundance of *P. denticola* and attenuated hypoxia-induced bone loss; fecal microbiota transplantation from nitrate-treated donors also improved the bone phenotype of the recipients. In vitro, nitrite inhibited *P. denticola* growth and altered the expression of markers of its glutamine-related metabolism. Together, these findings suggest that nitrate modulates the gut microbiota and glutamine-related metabolism during hypoxia, helping to preserve intestinal and skeletal homeostasis and attenuate bone loss. [31-33]Evidence that oral bacteria can promote extraoral inflammation through intestinal colonization and immune modulation provides a broader context for our findings involving *P. denticola*, an oral-associated species. However, our study did not establish ectopic intestinal colonization by *P. denticola* or determine whether nitrate reduces its oral abundance, limits its enrichment within the gut microbiota, or acts at both sites.

The mechanisms underlying chronic hypoxia-induced bone loss remain incompletely understood, and strategies for protecting bone during sustained hypoxic exposure remain limited.[34] Previous studies have implicated oxidative stress, hypoxic responses in bone cells, and cellular senescence in hypoxia-induced bone damage, and have explored corresponding pharmacological and physical interventions.[35,36,37,38] These studies highlight the importance of local responses in bone tissue. Moreover, how systemic inflammatory, metabolic, and intestinal factors influence bone remodeling during chronic hypoxia remains unclear. The gut–bone axis provides a framework for understanding these interorgan effects. Previous work has shown that microbial metabolites and gut-derived signals can affect skeletal and joint tissues.[13,39,3] Under hypoxia, the modifiable microbial–metabolic processes through which gut alterations affect bone cells remain unclear. Our study links hypoxia-associated gut changes to *P. denticola*, glutamine metabolism, and osteoclast function. The nitrate supplementation and FMT results further support a role for modifiable gut-associated factors in shaping the bone phenotype under hypoxia.

The FMT findings further support a functional role for the gut in nitrate-mediated bone protection. Previous studies have shown that the gut microbiota regulates bone remodeling through immune cell activity, short-chain fatty acids, and endocrine signaling. Studies of microbial metabolic cooperation and extracellular vesicles further suggest that the gut can influence distant musculoskeletal tissues through multiple routes.[9,11,40,41,42] Recent work on intestinal FXR–GLP-1 signaling also suggests that specific regulatory processes within the gut

can contribute to the protection of distant tissues.[39] Further microbiota profiling identified *P. denticola* as responsive to both hypoxia and nitrate supplementation, providing a basis for testing its contribution.

Supplementation with *P. denticola* exacerbated hypoxia-associated skeletal damage, providing functional evidence for its contribution to the bone phenotype. This effect was consistent with its increased relative abundance under hypoxia and decreased relative abundance following nitrate supplementation. Notably, nitrate improved the bone phenotype without significantly altering gut microbiota α-diversity compared with hypoxia alone. These findings suggest that α-diversity alone may not adequately reflect changes in specific taxa and microbial functions relevant to bone. Studies showing that environmental temperature affects bone mass through the gut microbiota and polyamine metabolism likewise point to microbial function as a mediator of environmental effects on the skeleton.[43] Therefore, the evaluation of gut-directed interventions under hypoxia should combine community-level measures with functional testing of specific taxa and metabolic activities and the assessment of host bone phenotypes.

Nitrate may affect microorganisms partly through nitrite and nitric oxide (NO) generated during nitrate reduction.[44,45,46] Recent studies of oral biofilms have shown that enhanced nitrate metabolism can coincide with shifts in community composition and a reduced abundance of some periodontitis-associated bacteria. These studies suggested that the antimicrobial activity of nitrate reduction products may contribute to these changes.[47] Therefore, we compared the effects of nitrate and nitrite on *P. denticola*. Under the culture conditions used in this study, compared with nitrate, nitrite resulted in more pronounced growth inhibition. Treatment with 2 mM nitrite was also accompanied by reduced glutamine synthetase activity and changes in the amino acid profile of the culture supernatant. Thus, the effects of nitrite may extend beyond growth inhibition to glutamine-related metabolic functions. However, the specific contribution of NO and whether comparable local exposure and metabolic effects occur in vivo require further investigation.

The altered amino acid profile of the culture supernatant provides a starting point for considering how microbial amino acid metabolism may influence host responses. Microbial processing of amino acids extends beyond nutrient conversion and may change the metabolic environment of distant tissues.[48-51] Recent studies have shown that dietary fiber redirects tryptophan metabolism through metabolic interactions among gut microbes, indicating that microbial function varies with the nutritional environment.[52,53] On the host side, phenylacetylglutamine, a microbial–host cometabolite linked to phenylalanine metabolism, can promote cellular senescence. Histidine-derived imidazole propionate can inhibit osteoblast differentiation and disrupt bone homeostasis.[54,15] These studies suggest that the effects of microbiota-associated changes in amino acid metabolism on bone homeostasis should be examined through both microbial metabolism and bone cell responses.

Our study extends this discussion to glutamine, an important metabolic substrate. Supplementation with *P. denticola* was accompanied by increased circulating glutamine levels, whereas nitrate intervention attenuated this increase. Under hypoxia, glutamine supplementation further exacerbated bone damage, while glutamine uptake increased during osteoclast differentiation. In addition to the signaling functions of amino acid-derived metabolites, our study examines the availability of amino acid substrates and their utilization by bone cells. Together, these findings suggest that changes in circulating glutamine levels and its utilization by osteoclasts may jointly contribute to dysregulated bone remodeling under hypoxia.

Building on these findings, we examined the roles of glutamine uptake and downstream metabolism in osteoclast differentiation under hypoxia. Previous work has established a basis for glutamine utilization in osteoclast formation and bone resorption.[55,56] In our study, *Slc1a5* deficiency improved the bone phenotype under hypoxia and reduced osteoclast differentiation in cells derived from *Slc1a5*-deficient mice.[57] Isotope tracing revealed that glutamine-derived carbon entered glutamate, α-KG, and tricarboxylic acid cycle intermediates. BPTES treatment and knockdown of Got2 or Glud1 were associated with reductions in α-KG levels and osteoclast differentiation. Together, evidence across these metabolic steps supports the involvement of Gln–α-KG metabolism in osteoclast differentiation under hypoxia. These findings link nitrate-associated changes in the gut and circulating metabolism to substrate utilization within bone cells. Considered alongside the microbiota intervention and circulating glutamine data, glutamine uptake and its conversion to α-KG in osteoclasts may represent a metabolic component of nitrate-associated bone protection.

α-KG can serve as a cosubstrate for histone demethylases. Thus, the conversion of glutamine to α-KG may influence the expression of genes involved in osteoclast differentiation by altering histone methylation.[58,59] Stegen *et al.* reported that α-KG produced through the serine synthesis pathway supports histone demethylation at the *Nfatc1* locus and promotes osteoclast maturation.[60] Under hypoxia, *Slc1a5* deficiency and α-KG supplementation were accompanied by changes in histone H3 lysine 27 trimethylation (H3K27me3), *Nfatc1* expression, and osteoclast differentiation, supporting a link between glutamine utilization and this transcriptional regulatory process. Glutamine also supplies substrates for amino acid and nucleotide synthesis. Previous studies have shown that α-KG supplementation does not restore osteoclast differentiation under all conditions, suggesting that different steps of glutamine metabolism may meet distinct cellular requirements.[16] Our rescue experiments suggest that, under hypoxic and *Slc1a5*-deficient conditions, α-KG-related processes may link glutamine utilization to osteoclast differentiation. These results connect metabolic changes with chromatin state; the specific histone demethylase involved remains to be determined.

These findings broaden our understanding of how nitrate preserves bone homeostasis during

hypoxia. Previous studies have shown that nitrate influences vascular function, mitochondrial efficiency, and glucose and lipid metabolism, indicating multilevel regulation of host physiological homeostasis.[25,26,27] Studies showing that nitrate promotes osteogenic differentiation and attenuates intestinal injury provide evidence for its effects in bone and the gut, respectively.[28,29,30] The improvement in trabecular microarchitecture with nitrate supplementation in hypoxia-exposed OVX mice extends the observed skeletal benefit to an estrogen-deficient setting (Supplementary Fig. 7). Whether the same microbial and metabolic mechanisms contribute to this benefit remains to be determined.Our findings further suggest that nitrate-mediated bone protection may partly involve changes in the gut and metabolic environments outside bone. Alongside improvements in markers of bone formation and resorption, gut-associated regulation of osteoclasts may represent one component of nitrate's skeletal effects. These results provide an experimental basis for exploring gut–host metabolic interactions as a target for preserving bone homeostasis during sustained hypoxic exposure.

Several important questions remain to be addressed in future studies. First, strain-specific functional interventions and in vivo metabolic tracing are needed to distinguish the relative microbial and host contributions to changes in glutamine. Second, cell type-specific models would help elucidate the effects revealed by global *Slc1a5* deficiency and determine whether cells outside the bone marrow also contribute to this process. Third, the in vivo conversion of nitrate to nitrite, local intestinal nitrite exposure, and the formation of reactive nitrogen species require more direct links to the in vitro responses of *P. denticola*. The specific enzymes and genomic loci involved in α-KG-associated chromatin changes also require genetic and functional validation. Finally, chronic hypoxia models do not capture the full range of environmental conditions and adaptive features experienced by high-altitude populations. The effective dose and long-term safety of nitrate, together with responses across different diets and baseline microbiota configurations, therefore require evaluation in human studies.

Overall, our findings support a role for nitrate in maintaining bone and metabolic homeostasis during chronic hypoxia through the modulation of gut–bone interactions. The functional effects of *P. denticola*, changes in circulating glutamine levels, and changes in Gln–α-KG metabolic responses in host osteoclasts provide convergent evidence for this protective effect. These findings extend the interpretation of hypoxia-induced bone injury from local responses in bone cells to interactions among the gut, microbiota, and host metabolism. They also provide mechanistic clues for understanding nitrate-mediated interorgan bone protection and for exploring intervention strategies against hypoxia-induced bone loss. Our findings also offer a perspective on how oral-associated microbes may influence skeletal health during chronic hypoxia and provide a basis for investigating whether nitrate-mediated bone protection involves oral–gut microbial interactions.

Materials and methods

1 Animals, ethics and study design

All animal procedures were approved by the Animal Care and Use Committee of Capital Medical University (approval no. AEEI-2025-911) and were performed in accordance with the relevant institutional guidelines. Eight-week-old male C57BL/6J mice were purchased from Beijing Vital River Laboratory Animal Technology Co., Ltd. (Beijing, China). The *Slc1a5*-knockout mouse line was obtained from Cyagen Biosciences (Suzhou) Inc. (Suzhou, China; product no. S-KO-04358) and maintained on a C57BL/6JCya background. Homozygous *Slc1a5*−/− mice were generated by intercrossing heterozygous mice, and age- and sex-matched wild-type littermates were used as controls. All mice were housed under specific pathogen-free conditions with ad libitum access to standard chow and drinking water.

The study comprised the following experimental cohorts. The nitrate-intervention cohort included the Control group maintained under normoxia (21% O_2), the Hypoxia group maintained under hypoxia (10% O_2) and the Hypoxia + Nit group maintained under hypoxia and provided drinking water containing 4 mmol L^{-1} nitrate. The microbiota-depletion cohort included the Control and antibiotic-treated (Abx) groups. The fecal microbiota transplantation (FMT) cohort included the Control, Hypoxia, Hypoxia + Nit, Hypoxia + FMT-H and Hypoxia + FMT-N groups. FMT-H and FMT-N denote transplantation of fecal microbiota obtained from hypoxia-exposed donors and nitrate-treated hypoxic donors, respectively. The Prevotella denticola intervention cohort included the Hypoxia, Hypoxia + P. denticola and Hypoxia + P. denticola + Nit groups. The glutamine-intervention cohort included the Hypoxia and Hypoxia + Gln groups. Mice in the Hypoxia + Gln group had ad libitum access to drinking water containing 4% (w/v; 4 g per 100 mL) glutamine (Beyotime Biotechnology, Shanghai, China) for three consecutive months, whereas mice in the Hypoxia group received regular drinking water under otherwise identical hypoxic conditions. The genetic-validation cohort comprised hypoxia-exposed wild-type and Slc1a5$^{-/-}$ mice. Detailed procedures for the individual interventions are described in the corresponding subsections below.

Within each experimental cohort, mice were allocated to equal-sized groups using block randomization. Investigators responsible for outcome assessment and data analysis were blinded to group allocation. All randomized animals were retained in the study and included in the final study population; no animals were excluded.

2. Chronic hypoxia and metabolic interventions

Mice assigned to the hypoxia groups were housed in a normobaric animal gas-control system (Attender140; Ningbo Huayi Ningchuang Intelligent Technology Co., Ltd., Ningbo, China) containing 10% O_2 continuously for 24 h per day for 3 months. Oxygen concentrations were continuously monitored. Normoxic control mice were maintained under ambient oxygen

conditions (21% O_2). Unless otherwise specified, all hypoxia-exposed cohorts underwent the same exposure protocol.

Sodium nitrate was dissolved in drinking water at a final concentration of 4 mmol L^{-1} and provided ad libitum as the sole drinking source. For glutamine supplementation, mice received drinking water containing 4% (w/v) glutamine (Beyotime Biotechnology, Shanghai, China) ad libitum. Both interventions were initiated on the first day of hypoxic exposure and continued throughout the 3-month experimental period. The corresponding hypoxic control groups received unsupplemented drinking water.

3. Antibiotic pretreatment and verification of microbiota depletion

Before fecal microbiota transplantation, mice received 200 μL of a freshly prepared antibiotic cocktail by oral gavage once daily for 14 days. The cocktail contained ampicillin sodium (0.5 mg mL^{-1}), neomycin sulfate (0.5 mg mL^{-1}), metronidazole (0.5 mg mL^{-1}) and vancomycin hydrochloride (0.25 mg mL^{-1}) in sterile water.

Fecal samples were collected before and after antibiotic treatment. Bacterial growth was assessed by fecal culture, and the V3–V4 region of the 16S rRNA gene was sequenced by LC-Bio Technologies (Hangzhou) Co., Ltd. (Hangzhou, China). Microbiota depletion was evaluated using observed species richness, the Shannon index and principal coordinates analysis based on unweighted UniFrac distances.

4. Fecal microbiota transplantation

Fresh fecal pellets were collected from five hypoxia-exposed donors and five nitrate-treated hypoxic donors. Equal masses of feces were pooled within each donor group and suspended in sterile, pre-reduced phosphate-buffered saline (PBS; 100 mg mL^{-1}). The suspensions were homogenized and centrifuged at low speed to remove coarse debris.

Following 14 days of antibiotic pretreatment, mice in the Hypoxia + FMT-H and Hypoxia + FMT-N groups received 200 μL of freshly prepared suspension from the corresponding donor group by oral gavage once daily for 3 months. Control, Hypoxia and Hypoxia + Nit mice received an equal volume of PBS on the same schedule without antibiotic pretreatment. Each of the five groups contained five mice ($n = 5$ per group).

5. Culture and administration of *Prevotella denticola*

Prevotella denticola JCM 13449 was obtained from Beijing BioBW Biotechnology Co., Ltd. (Beijing, China; accession no. bio-135295). The bacterium was cultured on EG agar supplemented with 5% sterile horse blood at 37 °C for 3–4 days under an anaerobic atmosphere of 80% N_2, 10% CO_2 and 10% H_2. Liquid cultures were prepared in pre-reduced EG medium without agar under the same conditions.

Actively growing bacteria were harvested by centrifugation, washed twice with sterile pre-reduced phosphate-buffered saline (PBS) and resuspended in the same buffer. Bacterial concentration was estimated by optical density and confirmed by viable colony counting. After antibiotic pretreatment, mice received 1×10^9 colony-forming units of viable *P. denticola* in 200 µL of sterile pre-reduced PBS by oral gavage once daily for 3 months. Vehicle-treated mice received an equal volume of sterile pre-reduced PBS. Where indicated, mice also received 4 mmol/L sodium nitrate in drinking water throughout the bacterial-administration period.

6. In vitro nitrate and nitrite treatment of *P. denticola*

P. denticola was cultured in pre-reduced EG medium containing sodium nitrate (0, 0.5, 1, 2, 10 or 100 mmol/L) or sodium nitrite (0, 0.5, 1, 2 or 10 mmol/L) under the anaerobic conditions described above. Bacterial growth was monitored for 48 h by measuring optical density at 600 nm.

For the assays shown in Fig. 5, nitrite-treated bacteria were plated on EG agar supplemented with 5% sterile horse blood for colony counting, stained with crystal violet to quantify biofilm formation, or prepared for scanning electron microscopy and fluorescent live/dead imaging. For gene-expression, glutamine synthetase activity and extracellular metabolite measurements, *P. denticola* was treated with 2 mmol/L sodium nitrite for 24 h. The expression of *glnA* and *glnB* was measured by reverse-transcription quantitative PCR. Glutamine synthetase activity was measured in bacterial lysates.Glutamine synthetase activity was normalized to the bacterial biomass of each sample before comparisons between groups,and culture supernatants were collected for targeted amino acid profiling.

7. Micro-computed tomography

Femurs were fixed in 4% paraformaldehyde and scanned using an Inveon CT/PET/SPECT system (Siemens, Germany) at 80 kV and 500 µA, with a 200-ms integration time and an 8.7-µm isotropic voxel size. The trabecular region of interest extended from 0.5 to 1.5 mm proximal to the distal femoral growth plate, excluding the cortical shell. Reconstructed images were analysed using CT-Analyser, CT-Volume and CT-Voxel (Bruker microCT, Kontich, Belgium). Bone mineral density (BMD), bone volume fraction (BV/TV), bone surface-to-tissue volume ratio (BS/TV), trabecular number (Tb.N), trabecular thickness (Tb.Th) and trabecular separation (Tb.Sp) were quantified.

8. Histology, histomorphometry and dynamic bone formation

Femurs were fixed in 4% paraformaldehyde for 48 h, decalcified in 10% ethylenediaminetetraacetic acid, embedded in paraffin and sectioned at 5 µm. Sections were stained with haematoxylin and eosin, Masson's trichrome or Trap. Trap-positive multinucleated cells containing at least three nuclei were classified as osteoclasts. Osteoclast number per bone

surface (N.Oc/BS), osteoclast surface per bone surface (Oc.S/BS) and Masson-positive bone matrix area were quantified using ImageJ.

For dynamic bone histomorphometry, calcein (30 mg kg^{-1}), prepared in 1 mol L^{-1} sodium bicarbonate, was administered by intraperitoneal injection 13 and 3 days before euthanasia. Fluorescent labels were analysed in undecalcified femoral sections. Mineral apposition rate (MAR) was calculated as the mean interlabel distance divided by the 10-day labelling interval. Bone formation rate per bone surface (BFR/BS) was calculated as MAR multiplied by mineralizing surface per bone surface (MS/BS).

9. Serum bone-turnover markers

Whole blood was collected at the experimental endpoint and allowed to clot at room temperature. Serum was separated by centrifugation and stored at −80 °C. Serum osteocalcin (OCN) and C-terminal telopeptide of type I collagen (CTX-1) were measured using enzyme-linked immunosorbent assay kits (Beyotime Biotechnology, China) according to the manufacturer's instructions.

10. Fecal metagenomic sequencing and microbial analysis

Fresh fecal samples were collected from the Control, Hypoxia and Hypoxia + Nit groups (n = 5 per group) under sterile conditions and stored at −80 °C. Microbial DNA was extracted and used to prepare multiplexed metagenomic libraries with the Ligation Sequencing Kit (Oxford Nanopore Technologies). Libraries were sequenced on MinION flow cells using an Mk1B device. Raw signals were base-called with Dorado7.6.8, and read quality and length were assessed using NanoPlot (v1.33.0). Taxonomic profiles were generated at the phylum, genus and species levels. Alpha diversity was assessed using the Chao1 estimator and Shannon index, and beta diversity by principal coordinates analysis of Bray–Curtis distances. Relative abundances were visualized using stacked bar, Circos and alluvial plots. Differentially abundant taxa were identified using linear discriminant analysis effect size (LEfSe).

11. Untargeted fecal metabolomics

Fecal samples from the Control, Hypoxia and Hypoxia + Nit groups (n = 5 per group) were analysed by untargeted metabolomics. Approximately 50 mg of each sample was homogenized with steel beads in 500 μL of ice-cold 80% methanol and incubated at −20 °C for 30 min. After centrifugation at 20,000 × g for 15 min, 400 μL of the supernatant was transferred to a fresh tube and centrifuged again under the same conditions. Equal aliquots of the extracts were pooled to prepare quality-control (QC) samples, which were analysed after every ten study samples.

Metabolites were separated on an ACQUITY UPLC T3 column (100 × 2.1 mm, 1.8 μm; Waters) using a Vanquish Flex ultrahigh-performance liquid chromatography system coupled

to an Orbitrap Exploris 240 mass spectrometer (Thermo Fisher Scientific). The mobile phases were water containing 5 mmol/L ammonium acetate and 5 mmol/L acetic acid (A) and acetonitrile (B), delivered over a 10-min gradient at 0.35 mL/min and 40 °C. Data were acquired separately in positive- and negative-ion modes using full-scan acquisition (m/z 70–1050; resolution 60,000 at m/z 200) and data-dependent MS/MS of the four most intense eligible precursor ions (resolution 15,000 at m/z 200).

Raw data were converted to mzXML format and processed using XCMS, CAMERA and metaX for peak detection, alignment and feature annotation. Metabolites were provisionally annotated by accurate-mass matching against KEGG and HMDB (mass tolerance <10 ppm), with isotope patterns and an in-house MS/MS spectral library providing additional evidence. Features missing from more than 80% of study samples or 50% of QC samples were excluded; remaining missing values were imputed by the k-nearest-neighbour method, followed by probabilistic quotient normalization. Principal component analysis, differential metabolite analysis and hierarchical clustering were performed, and KEGG pathway enrichment was assessed by a hypergeometric test.

12. Targeted amino acid metabolomics

Targeted amino acid profiling was performed on serum from two experimental cohorts: Control, Hypoxia, and Hypoxia + Nit; and Hypoxia, Hypoxia + P. denticola, and Hypoxia + P. denticola + Nit. Bacterial culture supernatants collected after nitrite exposure were also analysed. For sample preparation, 50 µL of serum or culture supernatant was mixed with 10 µL of aqueous sulfosalicylic acid and 10 µL of internal-standard solution, then brought to 500 µL with 0.1% formic acid in water. Samples were sonicated for 15 min and centrifuged at 20,000 × g for 15 min at 4 °C.

The supernatants were analysed using a Vanquish liquid chromatography system coupled to a TSQ Altis triple-quadrupole mass spectrometer (Thermo Fisher Scientific). Separation was performed on a Kinetex F5 column (5 µm, 4.6 × 250 mm) at 40 °C, with a 5-µL injection volume. The mobile phases were 10 mmol/L ammonium formate in water (A) and 10 mmol/L ammonium formate in methanol–water (9:1, v/v; B), both containing 0.1% formic acid. Data were acquired in positive electrospray-ionization mode using multiple-reaction monitoring. Target compounds were identified using authentic standards (Alta Scientific, Tianjin, China) and quantified using internal standards.

13. Isolation of bone marrow-derived macrophages and osteoclast differentiation

Bone marrow cells were flushed from the femurs and tibias of 8-week-old wild-type and *Slc1a5*−/− mice. After red blood cell lysis, cells were cultured for 24 h in α-minimum essential medium (α-MEM) supplemented with 10% fetal bovine serum and 1% penicillin–streptomycin to remove adherent stromal cells. Non-adherent bone marrow cells were collected and cultured

for 2 days in antibiotic-free α-MEM containing 25 ng/mL macrophage colony-stimulating factor (M-CSF).

Osteoclast differentiation was induced with 25 ng/mL M-CSF and 50 ng/mL receptor activator of nuclear factor-κB ligand (RANKL). Hypoxic cultures were maintained at 3% O_2, whereas control cultures were maintained at 21% O_2. Medium containing freshly prepared cytokines was replaced every 2 days until mature osteoclasts formed.

14. Intracellular glutamine measurement.

Osteoclast cultures were collected at the indicated differentiation time points or following V-9302 treatment. Cells were washed with ice-cold phosphate-buffered saline, counted and homogenized in 0.9% saline (200 μL per 10^6 cells) by sonication on ice. Homogenates were centrifuged at 10,000 × g for 15 min, and the supernatants were passed through 50-kDa ultrafiltration units at 10,000 × g for 15 min. Glutamine in the filtrates was measured using a colorimetric assay kit (E-BC-K853-M; Elabscience) according to the manufacturer's instructions. Absorbance was recorded at 450 nm before and after the final incubation, and glutamine content was calculated from a standard curve and expressed as μmol per 10^6 cells.

15. Trap and F-actin staining of cultured osteoclasts

Differentiated cells were washed three times with phosphate-buffered saline (PBS), fixed in 4% paraformaldehyde for 10 min and stained for tartrate-resistant acid phosphatase (Trap) at 37 °C for 1 h. Trap-positive multinucleated cells containing at least three nuclei were counted as mature osteoclasts. Entire wells were imaged, and osteoclast numbers were quantified using ImageJ.

For F-actin staining, mature osteoclasts were fixed in 4% paraformaldehyde, permeabilized with 0.1% Triton X-100 and incubated with fluorophore-conjugated phalloidin for 1 h. Nuclei were counterstained with DAPI for 5 min. Three randomly selected fields were imaged per well, and intact F-actin rings were quantified using ImageJ.

16. [U-$^{13}C_5$]glutamine tracing

Osteoclasts were incubated with 2 mmol/L [U-$^{13}C_5$]glutamine for 6 h. After labelling, cells were detached enzymatically and collected by centrifugation. Cell pellets were lyophilized, resuspended in 200 μL water, subjected to three freeze–thaw cycles in liquid nitrogen and sonicated for 10 min. An aliquot was retained for bicinchoninic acid protein quantification. The remaining homogenate (120 μL) was mixed with 480 μL methanol, sonicated for 10 min, incubated at −40 °C for 1 h and centrifuged at 12,000 r.p.m. for 15 min at 4 °C. The supernatants were dried and reconstituted in methanol/water (4:1, v/v).

Metabolites were separated using an Agilent 1290 Infinity II ultrahigh-performance liquid

chromatography system equipped with an Atlantis Premier BEH Z-HILIC or ACQUITY UPLC BEH C18 column and detected using an Orbitrap Exploris 120 mass spectrometer. Raw data were converted to mzXML format using ProteoWizard and processed using an in-house R workflow for peak detection, alignment and integration. Isotopologue distributions were expressed as mass distribution vectors.

17. Reverse-transcription quantitative PCR

Total RNA was extracted from cultured osteoclasts or *P. denticola* and reverse-transcribed into complementary DNA. Quantitative PCR was performed using a SYBR Green master mix and gene-specific primers. In mouse cells, the expression of *Acp5*, *Traf6*, *Ctsk*, *Nfatc1* and *Slc1a5* was normalized to *Actb*. In *P. denticola*, *glnA* and *glnB* expression was normalized to the bacterial reference gene. Relative expression was calculated using the $2^{-\Delta\Delta Ct}$ method. Primer sequences are provided in Supplementary Table 1.

18. Immunoblotting

Cells were washed with ice-cold phosphate-buffered saline and lysed in RIPA buffer containing protease and phosphatase inhibitors. Protein concentrations were determined using the bicinchoninic acid assay. Equal amounts of protein were separated by sodium dodecyl sulfate–polyacrylamide gel electrophoresis and transferred to polyvinylidene fluoride membranes. After blocking, membranes were incubated with primary antibodies overnight at 4 °C, followed by horseradish peroxidase-conjugated secondary antibodies. Signals were detected by enhanced chemiluminescence and quantified using ImageJ. β-actin and total histone H3 served as loading controls for whole-cell proteins and histone modifications, respectively.

19. Immunofluorescence staining

Paraffin-embedded femoral sections were deparaffinized, rehydrated and subjected to antigen retrieval. After blocking, sections were incubated with antibodies against ASCT2 and cathepsin K or H3K27me3, as indicated, overnight at 4 °C. Sections were then incubated with fluorophore-conjugated secondary antibodies, and nuclei were counterstained with DAPI. Images within each experiment were acquired using identical settings. Fluorescence intensity or positive area was quantified using ImageJ.

20. Antibodies

Primary antibodies included rabbit polyclonal anti-ASCT2/SLC1A5 (20350-1-AP; Proteintech, Wuhan, China), mouse monoclonal anti-NFATc1 (clone 7A6, sc-7294; Santa Cruz Biotechnology, Dallas, TX, USA), recombinant rabbit monoclonal anti-cathepsin K (clone EP9403, ab187647; Abcam, Cambridge, UK), recombinant mouse monoclonal anti-H3K4me3 (bsm-60087M; Bioss, Beijing, China), rabbit polyclonal anti-H3K9me3 (bs-53114R; Bioss), recombinant rabbit monoclonal anti-H3K27me3 (bsm-60656R; Bioss), rabbit polyclonal anti-

β-actin (20536-1-AP; Proteintech) and rabbit polyclonal anti-histone H3 (17168-1-AP; Proteintech). Normal rabbit IgG (30000-0-AP; Proteintech) served as the negative control for chromatin immunoprecipitation. Anti-H3K27me3 was used for immunoblotting, immunofluorescence staining and chromatin immunoprecipitation.

21. Chromatin immunoprecipitation quantitative PCR

After 72 h of treatment, osteoclast precursors were crosslinked with 1% formaldehyde, washed and collected by centrifugation at 1,000 × *g* for 5 min at 4 °C. Cell pellets were resuspended in lysis buffer containing 50 mmol/L Tris–HCl (pH 8.0), 150 mmol/L NaCl, 2 mmol/L EDTA, 1% Triton X-100, 0.5% sodium deoxycholate, 1% sodium dodecyl sulfate and protease inhibitors. Samples were incubated on ice for 10 min and sonicated to shear chromatin.

After centrifugation at 16,000 × *g* for 10 min at 4 °C, an aliquot of sheared chromatin was retained as the input control. The remaining chromatin was incubated with 5 μg anti-H3K27me3 antibody or an equal amount of normal rabbit IgG. Immunocomplexes were captured using Pierce Protein A/G Magnetic Beads. Following RNA and protein digestion, DNA was purified using Agencourt AMPure XP beads. H3K27me3 enrichment at three regions surrounding the *Nfatc1* transcription start site, designated TSS1–TSS3, was quantified using SYBR GreenER qPCR SuperMix Universal.

22. Statistical analysis

Quantitative data are presented as mean ± s.d. Cell experiments were performed independently at least three times. Statistical analyses were conducted using GraphPad Prism 8.0 (GraphPad Software, San Diego, CA, USA). Normally distributed data from two groups were compared using an unpaired two-sided Student's *t*-test, with Welch's correction when variances were unequal. Multiple groups were compared using one-way analysis of variance followed by Tukey's multiple-comparisons test. Experiments involving two independent variables were analysed using two-way analysis of variance followed by Tukey's multiple-comparisons test. Spearman's rank correlation was used to assess associations between bacterial taxa and metabolites. All tests were two-sided, and $P < 0.05$ was considered statistically significant. Sample sizes and statistical tests for individual experiments are specified in the figure legends.

Acknowledgements

This work was supported by Beijing Natural Science Foundation(L2610030); Beijing High-Level Innovation and Entrepreneurship Talent Support Program-Dengfeng Project (G202512061); China Science and Technology Talent and Platform Plan in Yunnan Province (202405AF140005); National Natural Science Foundation of China (81741106, 82401082, 82601909); Laboratory for Clinical Medicine, Capital Medical University, Beijing; Young Scientist Program of Beijing Stomatological Hospital, Capital Medical University (No. YSP202408). We specially thank the Laboratory for Clinical Medicine of Capital Medical University as well as the Core Facility Center of Capital Medical University for providing experimental equipment and technical support. We also thank American Journal Experts (AJE) for English language editing of this manuscript.

Conflict of Interests

The authors declare no competing interests.

Author Contributions

Jian Zhou conceived and designed the study and supervised the project. Zixiao Li, Yifan Xu, and Xu Zha performed the experiments, analyzed the data, and drafted the manuscript. Chenchen Zhou, Xiaoyu Li, Haoran Du, Kang Gao, Yibo Liu, Zhaoyao Qi, Xiaochen Fang, and Weihua Guo assisted with the experiments and data analysis. Xicheng Liu provided methodological guidance and critically revised the manuscript. Songlin Wang provided conceptual guidance. Jian Zhou revised and finalized the manuscript. Zixiao Li, Yifan Xu, and Xu Zha contributed equally to this work. All authors read and approved the final manuscript.

References

1. Tremblay, J. C., Ainslie, P. N. Global and country-level estimates of human population at high altitude. Proc. Natl Acad. Sci. USA 118, e2102463118 (2021).

2. Roach, R. C. et al. The 2018 Lake Louise Acute Mountain Sickness Score. High Alt. Med. Biol. 19, 4–6 (2018).

3. Zhu, S. et al. Hydrogen intervention attenuates chronic hypoxia-induced bone degeneration and multiorgan damage via modulation of the gut microbiota. Bone 203, 117718 (2026).

4. Zuo, H. et al. High-altitude exposure decreases bone mineral density and its relationship with gut microbiota: Results from the China multiethnic cohort (CMEC) study. Environ Res 215, 114206 (2022).

5. Utting, J. C. et al. Hypoxia inhibits the growth, differentiation and bone-forming capacity of rat osteoblasts. Exp. Cell Res. 312, 1693–1702 (2006).

6. Arnett, T. R. et al. Hypoxia is a major stimulator of osteoclast formation and bone resorption. J. Cell Physiol. 196, 2–8 (2003).

7. Miyauchi, Y. et al. HIF1α is required for osteoclast activation by estrogen deficiency in postmenopausal osteoporosis. Proc. Natl Acad. Sci. USA 110, 16568–16573 (2013).

8. Stegen, S., Carmeliet, G. Metabolic regulation of skeletal cell fate and function. Nat Rev Endocrinol 20, 399–413 (2024).

9. Li, J. Y. et al. Sex steroid deficiency-associated bone loss is microbiota dependent and prevented by probiotics. J. Clin. Invest. 126, 2049–2063 (2016).

10. Yu, M. et al. Ovariectomy induces bone loss via microbial-dependent trafficking of intestinal TNF+ T cells and Th17 cells. J. Clin. Invest. 131, e143137 (2021).

11. Tyagi, A. M. et al. The Microbial Metabolite Butyrate Stimulates Bone Formation via T Regulatory Cell-Mediated Regulation of WNT10B Expression. Immunity 49, 1116–1131.e7 (2018).
12. Lyu, Z., Hu, Y., Guo, Y., Liu, D. Modulation of bone remodeling by the gut microbiota: a new therapy for osteoporosis. Bone Res. 11, 31 (2023).
13. Lucas, S. et al. Short-chain fatty acids regulate systemic bone mass and protect from pathological bone loss. Nat. Commun. 9, 55 (2018).
14. Koh, A. et al. Microbially produced imidazole propionate impairs insulin signaling through mTORC1. Cell 175, 947–961.e17 (2018).
15. Park, S. G. et al. The microbial metabolite imidazole propionate dysregulates bone homeostasis by inhibiting AMP-activated protein kinase (AMPK) signaling. Commun. Biol. 7, 1644 (2024).
16. Hu, G. et al. Glutaminolysis provides nucleotides and amino acids to regulate osteoclast differentiation in mice. EMBO Rep. 25, 4515–4541 (2024).
17. Peng, R. et al. IL-17 promotes osteoclast-induced bone loss by regulating glutamine-dependent energy metabolism. Cell Death Dis 15, 111 (2024).
18. Lee, S. et al. Glutamine metabolite α-ketoglutarate acts as an epigenetic co-factor to interfere with osteoclast differentiation. Bone 145, 115836 (2021).
19. Bertels, J. C., He, G., Long, F. Metabolic reprogramming in skeletal cell differentiation. Bone Res. 12, 57 (2024).
20. Stegen, S. et al. Glutamine Metabolism in Osteoprogenitors Is Required for Bone Mass Accrual and PTH-Induced Bone Anabolism in Male Mice. J. Bone Miner. Res. 36, 604–

616 (2021).

21. Saag, K. G. et al. Romosozumab or alendronate for fracture prevention in women with osteoporosis. N. Engl. J. Med. 377, 1417–1427 (2017).

22. Cummings, S. R. et al. Vertebral fractures after discontinuation of denosumab: a post hoc analysis of the randomized placebo-controlled FREEDOM trial and its extension. J. Bone Miner. Res. 33, 190–198 (2018).

23. Lundberg, J. O., Carlström, M., Weitzberg, E. Metabolic Effects of Dietary Nitrate in Health and Disease. Cell Metab. 28, 9–22 (2018).

24. Carlström, M. Nitric oxide signaling in kidney regulation and cardiometabolic health. Nat Rev Nephrol 17, 575–590 (2021).

25. Kapil, V., Khambata, R. S., Robertson, A., Caulfield, M. J., Ahluwalia, A. Dietary nitrate provides sustained blood pressure lowering in hypertensive patients: a randomized, phase 2, double-blind, placebo-controlled study. Hypertension 65, 320–327 (2015).

26. Larsen, F. J. et al. Dietary inorganic nitrate improves mitochondrial efficiency in humans. Cell Metab. 13, 149–159 (2011).

27. Carlström, M. et al. Dietary inorganic nitrate reverses features of metabolic syndrome in endothelial nitric oxide synthase-deficient mice. Proc. Natl Acad. Sci. USA 107, 17716–17720 (2010).

28. Li, X. et al. Salivary nitrate prevents osteoporosis by regulating bone marrow mesenchymal stem cells proliferation and differentiation. J. Orthop. Transl. 45, 188–196 (2024).

29. Hu, L. et al. Nitrate ameliorates dextran sodium sulfate-induced colitis by regulating the

homeostasis of the intestinal microbiota. Free Radic. Biol. Med. 152, 609–621 (2020).

30. Xu, Y. et al. A preventative role of nitrate for hypoxia-induced intestinal injury. Free Radic. Biol. Med. 213, 457–469 (2024).

31.Atarashi, K. et al. Ectopic colonization of oral bacteria in the intestine drives TH1 cell induction and inflammation. Science 358, 359–365 (2017)

32.Kitamoto, S. et al. The Intermucosal Connection between the Mouth and Gut in Commensal Pathobiont-Driven Colitis. Cell 182, 447–462.e14 (2020).

33.Huang, T. et al. Integrative analysis of oral microbiota and its gut transmission with host immunity in term pregnancy. npj Biofilms Microbiomes 12, 161 (2026).

34. Brent, M. B., Simonsen, U., Thomsen, J. S., Brüel, A. Effect of Acetazolamide and Zoledronate on Simulated High Altitude-Induced Bone Loss. Front. Endocrinol. 13, 831369 (2022).

35. Morten, K. J., Badder, L., Knowles, H. J. Differential regulation of HIF-mediated pathways increases mitochondrial metabolism and ATP production in hypoxic osteoclasts. J. Pathol. 229, 755–764 (2013).

36. Wang, S. et al. Senolytic cocktail dasatinib and quercetin attenuates chronic high altitude hypoxia associated bone loss in mice. Sci. Rep. 14, 30417 (2024).

37. Hao, X. et al. Bone Deterioration in Response to Chronic High-Altitude Hypoxia Is Attenuated by a Pulsed Electromagnetic Field Via the Primary Cilium/HIF-1α Axis. J. Bone Miner. Res. 38, 597–614 (2023).

38. Wang, D. et al. Whole-body vibration protects against chronic high-altitude hypoxic bone loss by regulating the nitric oxide/HIF-1α axis in osteoblasts. FASEB J 39, e70385

(2025).

39. Yang, Y. et al. Osteoarthritis treatment via the GLP-1-mediated gut-joint axis targets intestinal FXR signaling. Science 388, eadt0548 (2025).

40. Yan, J. et al. Gut microbiota induce IGF-1 and promote bone formation and growth. Proc. Natl Acad. Sci. USA 113, E7554–E7563 (2016).

41. Chen, M. et al. Bifidobacterium animalis subsp. lactis A6 ameliorates bone and muscle loss via modulating gut microbiota composition and enhancing butyrate production. Bone Res. 13, 28 (2025).

42. Guan, Z. et al. Akkermansia muciniphila attenuates intervertebral disc degeneration via extracellular vesicle-mediated delivery of the effector protein B2UKX5. Bone Res. 14, 56 (2026).

43. Chevalier, C. et al. Warmth Prevents Bone Loss Through the Gut Microbiota. Cell Metab. 32, 575–590.e7 (2020).

44. Rosier, B. T. et al. The Importance of Nitrate Reduction for Oral Health. J. Dent. Res. 101, 887–897 (2022).

45. Rosier, B. T. et al. Nitrate reduction capacity of the oral microbiota is impaired in periodontitis: potential implications for systemic nitric oxide availability. Int. J. Oral Sci. 16, 1 (2024).

46. Rojas-Tapias, D. F. et al. Inflammation-associated nitrate facilitates ectopic colonization of oral bacterium Veillonella parvula in the intestine. Nat. Microbiol. 7, 1673–1685 (2022).

47. Mazurel, D. et al. Nitrate and a nitrate-reducing Rothia aeria strain as potential prebiotic

945 or synbiotic treatments for periodontitis. npj Biofilms Microbiomes 9, 40 (2023).
946 48. Serger, E. et al. The gut metabolite indole-3 propionate promotes nerve regeneration and
947 repair. Nature 607, 585–592 (2022).
948 49. Jiang, Z. et al. Human gut microbial aromatic amino acid and related metabolites prevent
949 obesity through intestinal immune control. Nat. Metab. 7, 808–822 (2025).
950 50. Saeedi Saravi, S. S. et al. Gut microbiota-dependent increase in phenylacetic acid induces
951 endothelial cell senescence during aging. Nat. Aging 5, 1025–1045 (2025).
952 51. Saha, P. P. et al. Gut microbe-generated phenylacetylglutamine is an endogenous allosteric
953 modulator of β2-adrenergic receptors. Nat. Commun. 15, 6696 (2024).
954 52. Sinha, A. K. et al. Dietary fibre directs microbial tryptophan metabolism via metabolic
955 interactions in the gut microbiota. Nat. Microbiol. 9, 1964–1978 (2024).
956 53. Starke, S. et al. Amino acid auxotrophies in human gut bacteria are linked to higher
957 microbiome diversity and long-term stability. ISME J. 17, 2370–2380 (2023).
958 54. Yang, H. et al. Gut microbial-derived phenylacetylglutamine accelerates host cellular
959 senescence. Nat. Aging 5, 401–418 (2025).
960 55. Indo, Y. et al. Metabolic regulation of osteoclast differentiation and function. J. Bone
961 Miner. Res. 28, 2392–2399 (2013).
962 56. Rohatgi, N. et al. BAP1 promotes osteoclast function by metabolic reprogramming. Nat.
963 Commun. 14, 5923 (2023).
964 57. Sharma, D., Yu, Y., Shen, L., Zhang, G. F., Karner, C. M. SLC1A5 provides glutamine
965 and asparagine necessary for bone development in mice. Elife 10, e71595 (2021).
966 58. Chakraborty, A. A. et al. Histone demethylase KDM6A directly senses oxygen to control

chromatin and cell fate. Science 363, 1217–1222 (2019).

59. Batie, M. et al. Hypoxia induces rapid changes to histone methylation and reprograms chromatin. Science 363, 1222–1226 (2019).

60. Stegen, S., Moermans, K., Stockmans, I., Thienpont, B., Carmeliet, G. The serine synthesis pathway drives osteoclast differentiation through epigenetic regulation of NFATc1 expression. Nat. Metab. 6, 141–152 (2024).

Figure Legends

Fig. 1 Nitrate supplementation alleviates hypoxia-induced bone loss in mice.

a Schematic illustration of the experimental design. C57BL/6J mice were maintained under normoxic conditions (21% O_2; Control), hypoxic conditions (10% O_2; Hypoxia), or hypoxic conditions supplemented with nitrate (10% O_2 + nitrate; Hypoxia+Nit) for 3 months. b Changes in body weight during the experimental period. c–f Quantification of bone mineral density (BMD), bone volume fraction (BV/TV), bone surface-to-tissue volume ratio (BS/TV) and trabecular number (Tb.N) in femurs from the indicated groups. g Representative computed tomography (CT) images of femurs. h Representative calcein-labeled fluorescence images of femoral sections showing bone formation. Scale bars, 50 μm. i Representative hematoxylin and eosin (H&E)-stained femoral sections. j Representative Masson's trichrome-stained femoral sections. For i and j, the scale bars are 500 μm for overview images and 200 μm for inset images. k Representative tartrate-resistant acid phosphatase (Trap)-stained femoral sections. Scale bars are 500 μm for overview images and 100 μm for inset images. l Quantification of the collagen/bone matrix area. m Quantification of osteoclast surface per bone surface (Oc.S/BS). n Serum osteocalcin (OCN) concentrations. o Serum C-terminal telopeptide of type I collagen (CTX-1) concentrations. p Quantification of the mineral apposition rate (MAR) based on the calcein-labeled sections shown in h. q Quantification of the bone formation rate per bone surface (BFR/BS) on the basis of the calcein-labeled sections shown in h. Data are presented as the mean ± s.d. The sample size was n = 6 per group for b–o and n = 3 per group for p and q. Statistical significance was assessed by analysis of variance (ANOVA). $*P < 0.05$, $**P < 0.01$, $***P < 0.001$

Fig. 2 Fecal microbiota transplantation from nitrate-treated donors alleviates hypoxia-induced bone loss.

a Representative images of fecal bacterial cultures from control and antibiotic-treated (Abx) mice. b Observed species richness and c Shannon diversity index of the fecal microbiota. d Principal coordinate analysis (PCoA) based on the unweighted UniFrac distance matrix. e Changes in body weight during the experimental period. f Representative computed tomography (CT) images of femurs from control, hypoxia, hypoxia+Nit, hypoxia+FMT-H and hypoxia+FMT-N mice. FMT-H denotes FMT from hypoxia-exposed donors, whereas FMT-N denotes FMT from nitrate-treated donors. g–j Quantification of bone mineral density (BMD), bone surface-to-tissue volume ratio (BS/TV), bone volume fraction (BV/TV) and trabecular number (Tb.N), respectively. k Representative hematoxylin and eosin (H&E)-stained femoral sections. Overview images are shown with corresponding inset images; scale bars, 500 μm for overview images and 200 μm for inset images. l Serum concentrations of C-terminal telopeptide of type I collagen (CTX-1). m Representative Masson's trichrome-

stained femoral sections. Overview images are shown with corresponding inset images; scale bars, 500 μm for overview images and 200 μm for inset images. n Quantification of the bone matrix area. o Trap-stained femoral sections. Overview images are shown with corresponding inset images; scale bars, 500 μm for overview images and 100 μm for inset images. p Quantification of osteoclast surface per bone surface (Oc.S/BS). Data are presented as the mean ± s.d. The sample size was n = 4 per group for b–d;n = 5 per group for e–l; n = 3 per group for n; and n = 5 per group for p. Statistical significance was assessed by two-way analysis of variance (ANOVA) for e and one-way ANOVA for b, c and g–p. *$P < 0.05$, **$P < 0.01$ and ***$P < 0.001$.

Fig. 3 Nitrate supplementation reshaped the gut microbiota and alleviated *Prevotella denticola*-associated bone loss in hypoxic mice.

a Chao1 estimator and b Shannon diversity index of the fecal microbiota in control, hypoxia and hypoxia+Nit mice. c Principal coordinate analysis (PCoA) based on the Bray–Curtis distance matrix. d Circos plot showing the relative contributions of bacterial phyla to the microbiota profiles of the indicated groups. e Alluvial plot showing the distribution of bacterial taxa from the group level to the phylum and genus levels. f Relative abundance of the predominant bacterial phyla in the indicated groups. g Linear discriminant analysis effect size (LEfSe) analysis showing differentially abundant bacterial species among the indicated groups. h Firmicutes-to-Bacteroidetes ratio. i–l Metagenomic sequencing-based quantification of the relative abundance of *Prevotella denticola*, *Prevotella sp. Rep29*, *Prevotella dentalis* and *Prevotella intermedia*, respectively. m Representative computed tomography (CT) images of femurs from Hypoxia, Hypoxia+P.d and Hypoxia+P.d+Nit mice. Hypoxia+P.d denotes hypoxia-exposed mice supplemented with *P. denticola*, whereas hypoxia+P.d+Nit denotes hypoxia-exposed mice supplemented with both *P. denticola* and nitrate. n Representative Masson's trichrome-stained femoral sections. Overview images and corresponding inset images are shown; scale bars, 500 μm for overview images and 200 μm for inset images. O Representative Trap-stained femoral sections. Overview images and corresponding inset images are shown; scale bars, 500 μm for overview images and 100 μm for inset images. p Quantification of osteoclast surface per bone surface (Oc.S/BS). Data are presented as the mean ± s.d.; n = 5 per group. Statistical significance was assessed by one-way analysis of variance (ANOVA). *$P < 0.05$, **$P < 0.01$ and ***$P < 0.001$.

Fig. 4 Nitrate supplementation modulates hypoxia-associated metabolic alterations and amino acid profiles in mice supplemented with *P. denticola*

a Partial least-squares discriminant analysis (PLS-DA) score plot of untargeted fecal metabolomic profiles. b, c Volcano plots of differential fecal metabolites in hypoxia versus control (b) and hypoxia+Nit versus hypoxia (c). Red and blue indicate increased and decreased abundance, respectively; gray indicates metabolites below the plotted thresholds. d Log_2-

transformed abundance of fecal Thr–Ala–Gln–Glu. e Heatmap of selected differential fecal metabolites, displayed as row-wise z scores. f KEGG pathway enrichment of differential fecal metabolites; bubble size indicates the number of mapped metabolites, and color indicates the adjusted P value. g Heatmap of serum amino acid profiles, displayed as row-wise z scores. h–m Serum concentrations of glutamine (Gln; h), glutamate (Glu; i), the combined signal of sarcosine, alanine and β-alanine (Sar & Ala & BAla; j), lysine (Lys; k), asparagine (Asn; l) and aspartate (Asp; m). n Spearman correlations between bacterial species abundances and fecal metabolites. Red and blue indicate positive and negative correlations, respectively; bubble size represents the absolute correlation coefficient. Yellow outlines highlight *P. denticola* and Thr–Ala–Gln–Glu. o, p Associations of *P. denticola* abundance with the fecal Thr–Ala–Gln–Glu composite z score (o) and serum glutamine concentration (p). Lines show linear fits; Pearson r values are displayed in the panels. q–s serum concentrations of glutamine (q), the combined Sar & Ala & BAla signal (r) and aspartate (s) in hypoxia-exposed mice without supplementation, with *P. denticola* supplementation (Hypoxia+P.d), or with *P. denticola* and nitrate cosupplementation (Hypoxia+P.d+Nit). Nit denotes nitrate supplementation. Bars show the mean ± s.d.; points represent individual mice. For a–n, n = 5 mice per group; for o and p, n = 15 mice; for q–s, n = 5 mice per group. Panel d was analysed using one-way ANOVA. Group comparisons in h–m and q–s were analysed using one-way ANOVA followed by Tukey's multiple-comparisons test. $*P < 0.05$; ns, not significant.

Fig. 5 Effects of nitrite on *Prevotella denticola* growth and nitrite-induced changes in amino acid metabolism.

a, b Relative mRNA expression of *glnA* (a) and *glnB* (b) in untreated and nitrite-treated *P. denticola*. c Glutamine synthetase activity. d Three-dimensional principal component analysis (PCA) of targeted amino acid profiles in bacterial culture supernatants. e Volcano plot showing changes in extracellular metabolite abundance after nitrite treatment relative to untreated controls. The axes show $\log_2$ fold change and $-\log_{10}$ of the Benjamini–Hochberg-adjusted q value. f Heatmap of selected extracellular amino acids, displayed as row-wise z scores. g Kyoto Encyclopedia of Genes and Genomes (KEGG) pathway enrichment analysis of differentially abundant metabolites; bubble size indicates the number of mapped compounds, and colour indicates the P value. h Chord diagram linking differentially abundant metabolites to enriched pathways. The compound rings indicate the direction and magnitude of abundance changes, and the pathway ring indicates pathway categories. i–n Concentrations of L-glutamic acid (i), L-glutamine (j), L-asparagine (k), β-alanine (l), L-serine (m) and L-tyrosine (n) in bacterial culture supernatants. For a–n, cultures were left untreated or treated with 2 mM nitrite for 24 h. o Representative agar plates showing bacterial growth after treatment with the indicated nitrite concentrations. p Representative crystal violet staining of bacterial biofilms. q Representative scanning electron microscopy images of bacteria treated with the indicated nitrite

concentrations. r Representative live/dead fluorescence images; green and red signals indicate live and dead bacteria, respectively.(scale bars=500 μm) For the quantitative assays in a–n, n = 3 per group. Bars show the mean ± s.d., and symbols indicate individual measurements. Two-group comparisons in a–c and i–n were analysed using unpaired two-sided Student's t-tests. *$P < 0.05$, **$P < 0.01$.

Fig. 6 Glutamine aggravates hypoxia-induced bone loss, and inhibition of glutamine uptake attenuates osteoclastogenesis.

a Representative microcomputed tomography (micro-CT) images of distal femurs from C57BL/6J mice exposed to hypoxia (10% O_2) with or without glutamine supplementation for 3 months. b, c Representative femoral sections stained with Masson's trichrome (b) and Trap (c). The lower panels show enlarged views of the boxed regions. d–g Quantification of bone mineral density (BMD; d), the bone surface-to-tissue volume ratio (BS/TV; e), the bone volume fraction (BV/TV; f) and the trabecular number (Tb.N; g). h Quantification of osteoclast surface per bone surface (Oc.S/BS). i Glutamine uptake on days 0, 3 and 7 of osteoclast differentiation under control and hypoxic conditions. j Quantification of glutamine uptake on day 7. k Heatmap showing the relative mRNA expression of osteoclastogenesis- and glutamine metabolism-related genes under control an University of Pennsylvaniad hypoxic conditions. l Representative immunofluorescence images showing ASCT2 (red) and cathepsin K (CTSK; green) expression in bone sections from control and hypoxic mice. Nuclei were counterstained with DAPI (blue). m Representative immunoblots of ASCT2 and CTSK in osteoclasts differentiated under control or hypoxic conditions, with β-actin as the loading control. n, o Quantification of ASCT2 (n) and CTSK (o) protein expression. p Representative Trap staining of osteoclasts differentiated under control or hypoxic conditions. q Quantification of Trap-positive multinucleated cells ($Trap^+$ MNCs) per well in p. r Glutamine uptake in osteoclasts treated with or without V-9302. s Representative Trap staining of osteoclasts cultured with the indicated concentrations of glutamine (0, 1, 2 or 4 mM) or with 2 mM glutamine plus V-9302. t Quantification of $Trap^+$ MNCs per well in s. u RT–qPCR analysis of *Trap*, *Traf6*, *Ctsk* and *Nfatc1* expression in the indicated groups. v Representative immunoblots of *NFATc1* in osteoclasts cultured with the indicated concentrations of glutamine or with 2 mM glutamine plus V-9302, with β-actin as the loading control. Data are presented as the mean ± SD or as box plots showing the median, interquartile range and minimum-to-maximum values. Each symbol represents one biologically independent mouse or independent experiment. *$P < 0.05$, **$P < 0.01$ and ***$P < 0.001$.

Fig. 7 ASCT2 deficiency preserves bone mass under hypoxia and impairs glutamine-dependent osteoclastogenesis.

a Representative microcomputed tomography (micro-CT) images of distal femurs from hypoxia-exposed wild-type (WT) and $Slc1a5^{-/-}$ mice. b–e Quantification of bone mineral

density (BMD; b), bone volume fraction (BV/TV; c), bone surface-to-tissue volume ratio (BS/TV; d) and trabecular number (Tb.N; e). f Trap staining and F-actin ring staining of osteoclast cultures derived from WT and *Slc1a5*$^{-/-}$ mice. g, h Numbers of Trap -positive multinucleated osteoclasts (g) and F-actin rings (h) per well. i Heatmap of relative mRNA expression of osteoclast-related genes and Slc1a5 in WT and *Slc1a5*$^{-/-}$ cultures. j Representative immunoblots of NFATc1, ASCT2 and cathepsin K (CTSK), with β-actin as the loading control. k, l Quantification of NFATc1 (k) and CTSK (l) protein expression. m Schematic of [U-$^{13}C_5$]glutamine tracing through glutamate and α-ketoglutarate (α-KG), showing oxidative tricarboxylic acid cycle metabolism, reductive carboxylation and glutathione metabolism. n Fractions of selected labeled isotopologues of glutamine-derived metabolites. o–q Mass isotopologue distributions of glutamine (o), glutamate (p) and α-KG (q). r Schematic of α-KG supplementation during osteoclast differentiation. s Heatmap of relative mRNA expression of osteoclast-related genes in WT and *Slc1a5*$^{-/-}$ cultures treated with vehicle or α-KG. t Representative Trap and F-actin ring staining in the indicated groups. u Number of Trap -positive multinucleated cells per well. v Representative immunoblots of H3K4me3, H3K9me3 and H3K27me3, with total histone H3 as the loading control. w Representative H3K27me3 immunofluorescence images of femoral sections from WT and *Slc1a5*$^{-/-}$ mice. Dashed lines delineate trabecular bone. x Chromatin immunoprecipitation–quantitative PCR analysis of H3K27me3 enrichment at three regions surrounding the *Nfatc1* transcription start site (TSS1–TSS3); IgG served as the negative control. For the in vivo experiments (a–e, w), n = 5 mice per group. For the cell-based experiments (f–l, n–q, s–v, x), n = 3 independent experiments per group. Two-group comparisons in b–e, g–i, k and l were analysed by one-way ANOVA. The genotype × α-KG experiments in s and u, and the analysis at each assayed TSS region in x, were analysed by two-way ANOVA followed by Tukey's multiple-comparisons test. Each gene in the heatmaps was analysed separately. *$P < 0.05$, **$P < 0.01$ and ***$P < 0.001$.

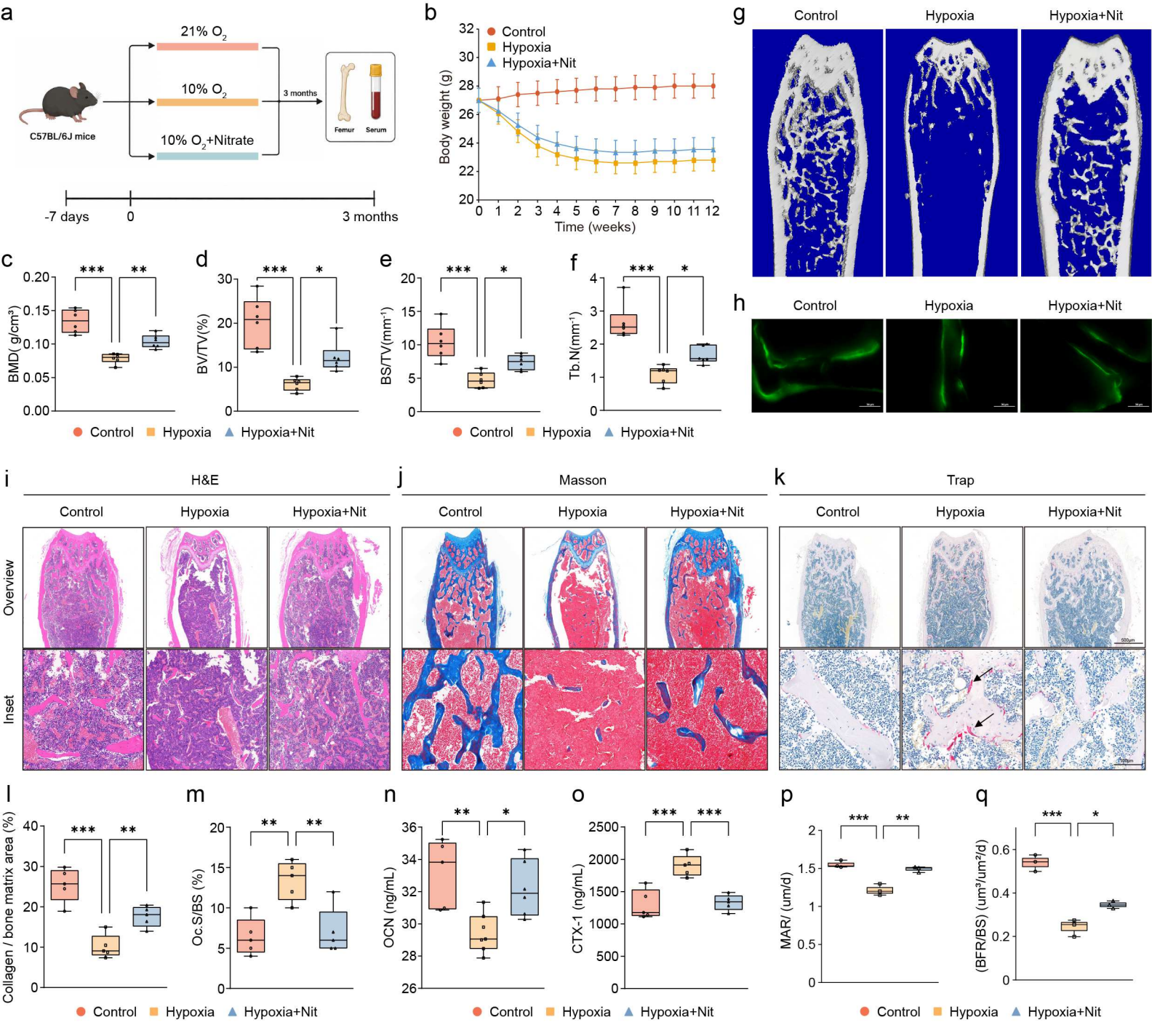
a
21% O2
10% O2
10% O2+Nitrate
3 months
C57BL/6J mice
Femur
Serum
-7 days
0
3 months
b
Control
Hypoxia
Hypoxia+Nit
Body weight (g)
Time (weeks)
g
Control
Hypoxia
Hypoxia+Nit
h
Control
Hypoxia
Hypoxia+Nit
c
BMD(g/cm³)
d
BV/TV(%)
e
BS/TV(mm⁻¹)
f
Tb.N(mm⁻¹)
Control
Hypoxia
Hypoxia+Nit
i
H&E
Control
Hypoxia
Hypoxia+Nit
Overview
Inset
j
Masson
Control
Hypoxia
Hypoxia+Nit
k
Trap
Control
Hypoxia
Hypoxia+Nit
l
Collagen / bone matrix area (%)
m
Oc.S/BS (%)
n
OCN (ng/mL)
o
CTX-1 (ng/mL)
p
MAR/ (um/d)
q
(BFR/BS) (um³/um²/d)
Control
Hypoxia
Hypoxia+Nit

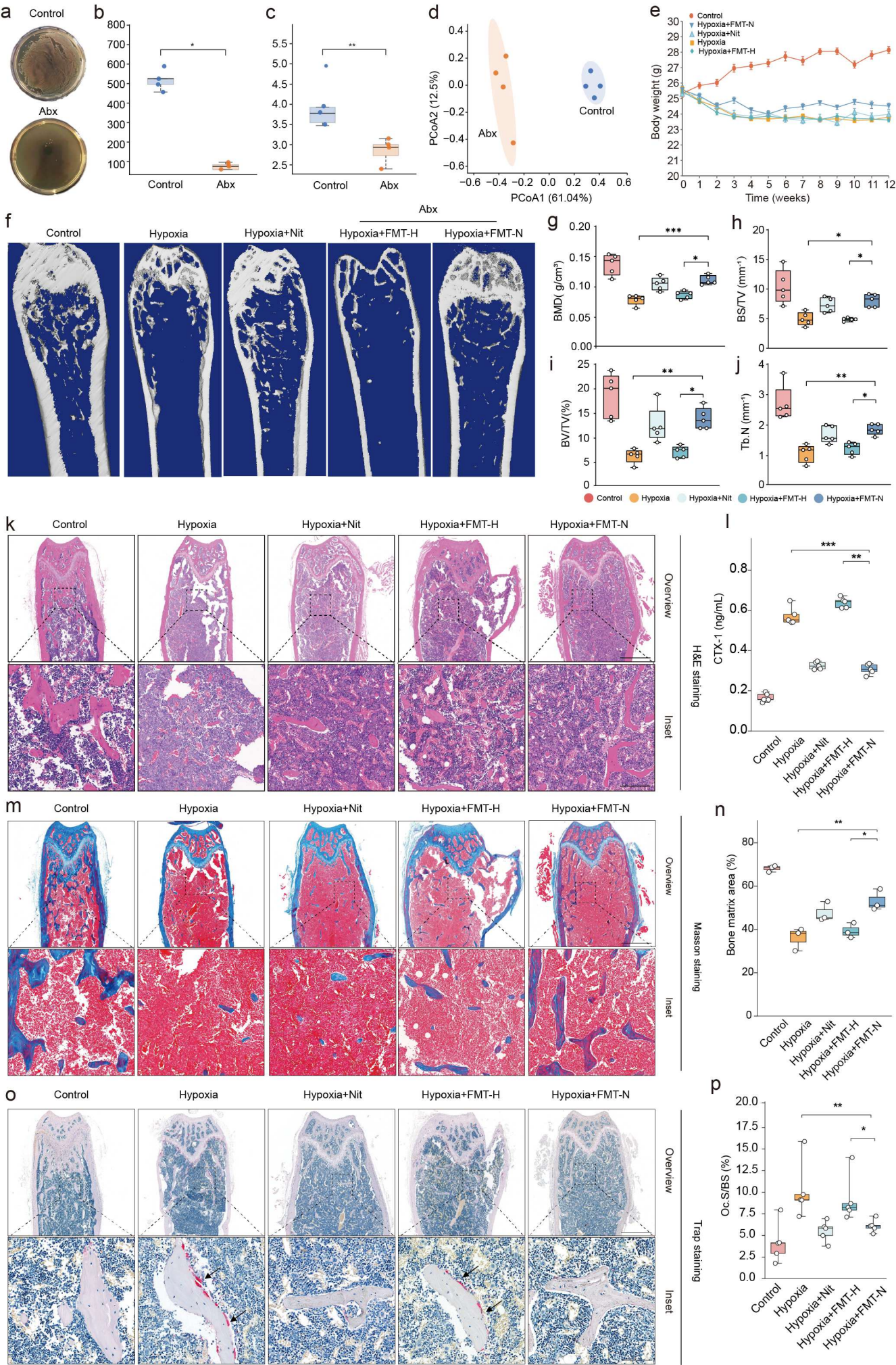
a
Control
Abx
b
Control
Abx
c
Control
Abx
d
PCoA2 (12.5%)
PCoA1 (61.04%)
Abx
Control
e
Control
Hypoxia+FMT-N
Hypoxia+Nit
Hypoxia
Hypoxia+FMT-H
Body weight (g)
Time (weeks)
f
Abx
Control
Hypoxia
Hypoxia+Nit
Hypoxia+FMT-H
Hypoxia+FMT-N
g
BMD(g/cm³)
h
BS/TV (mm⁻¹)
i
BV/TV(%)
j
Tb.N (mm⁻¹)
Control
Hypoxia
Hypoxia+Nit
Hypoxia+FMT-H
Hypoxia+FMT-N
k
Control
Hypoxia
Hypoxia+Nit
Hypoxia+FMT-H
Hypoxia+FMT-N
Overview
Inset
H&E staining
l
CTX-1 (ng/mL)
Control
Hypoxia
Hypoxia+Nit
Hypoxia+FMT-H
Hypoxia+FMT-N
m
Control
Hypoxia
Hypoxia+Nit
Hypoxia+FMT-H
Hypoxia+FMT-N
Overview
Inset
Masson staining
n
Bone matrix area (%)
Control
Hypoxia
Hypoxia+Nit
Hypoxia+FMT-H
Hypoxia+FMT-N
o
Control
Hypoxia
Hypoxia+Nit
Hypoxia+FMT-H
Hypoxia+FMT-N
Overview
Inset
Trap staining
p
Oc.S/BS (%)
Control
Hypoxia
Hypoxia+Nit
Hypoxia+FMT-H
Hypoxia+FMT-N

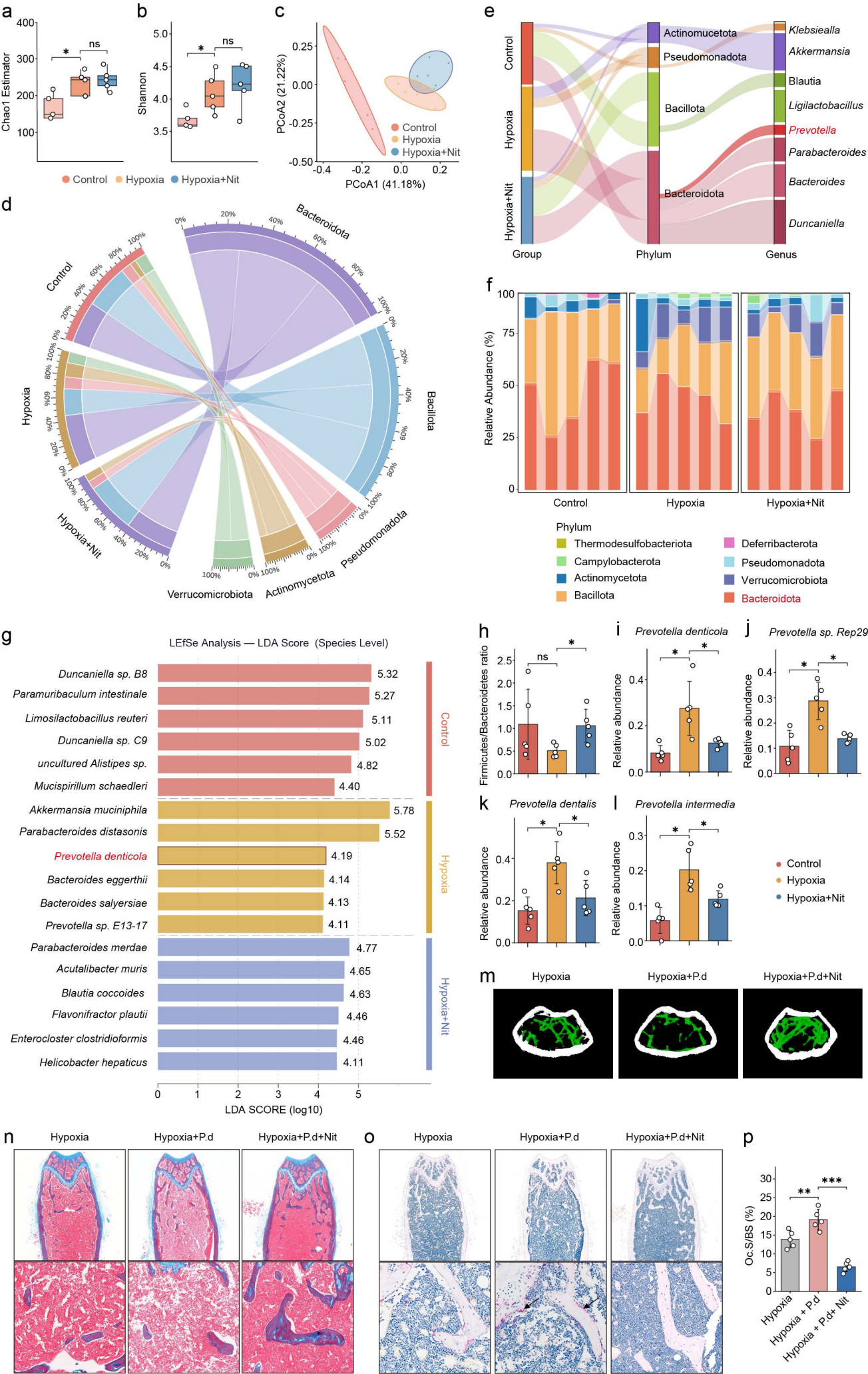
a
Chao1 Estimator
ns
Control
Hypoxia
Hypoxia+Nit
b
Shannon
c
PCoA2 (21.22%)
PCoA1 (41.18%)
e
Group
Phylum
Genus
Actinomucetota
Pseudomonadota
Bacillota
Bacteroidota
Klebsiealla
Akkermansia
Blautia
Ligilactobacillus
Prevotella
Parabacteroides
Bacteroides
Duncaniella
d
f
Relative Abundance (%)
Phylum
Thermodesulfobacteriota
Campylobacterota
Actinomycetota
Bacillota
Deferribacterota
Pseudomonadota
Verrucomicrobiota
Bacteroidota
g
LEfSe Analysis — LDA Score (Species Level)
Duncaniella sp. B8 5.32
Paramuribaculum intestinale 5.27
Limosilactobacillus reuteri 5.11
Duncaniella sp. C9 5.02
uncultured Alistipes sp. 4.82
Mucispirillum schaedleri 4.40
Akkermansia muciniphila 5.78
Parabacteroides distasonis 5.52
Prevotella denticola 4.19
Bacteroides eggerthii 4.14
Bacteroides salyersiae 4.13
Prevotella sp. E13-17 4.11
Parabacteroides merdae 4.77
Acutalibacter muris 4.65
Blautia coccoides 4.63
Flavonifractor plautii 4.46
Enterocloster clostridioformis 4.46
Helicobacter hepaticus 4.11
LDA SCORE (log10)
h
Firmicutes/Bacteroidetes ratio
i
Prevotella denticola
j
Prevotella sp. Rep29
k
Prevotella dentalis
l
Prevotella intermedia
Relative abundance
m
Hypoxia
Hypoxia+P.d
Hypoxia+P.d+Nit
n
o
p
Oc.S/BS (%)
Hypoxia
Hypoxia + P.d
Hypoxia + P.d+ Nit

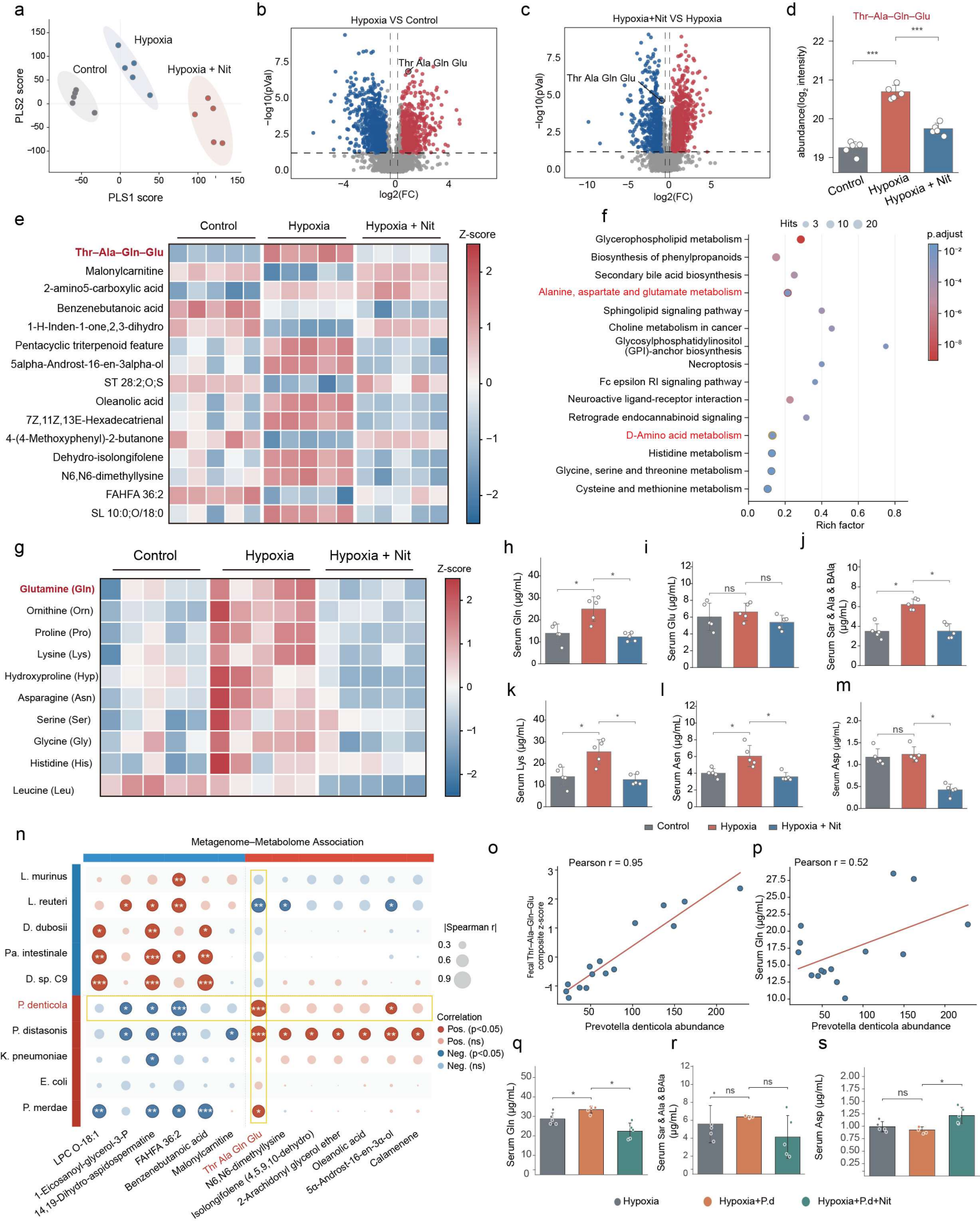
a
Hypoxia
Control
Hypoxia + Nit
PLS2 score
PLS1 score
b
Hypoxia VS Control
Thr Ala Gln Glu
−log10(pVal)
log2(FC)
c
Hypoxia+Nit VS Hypoxia
Thr Ala Gln Glu
−log10(pVal)
log2(FC)
d
Thr–Ala–Gln–Glu
abundance(log2 intensity)
Control
Hypoxia
Hypoxia + Nit
e
Control
Hypoxia
Hypoxia + Nit
Z-score
Thr–Ala–Gln–Glu
Malonylcarnitine
2-amino5-carboxylic acid
Benzenebutanoic acid
1-H-Inden-1-one,2,3-dihydro
Pentacyclic triterpenoid feature
5alpha-Androst-16-en-3alpha-ol
ST 28:2;O;S
Oleanolic acid
7Z,11Z,13E-Hexadecatrienal
4-(4-Methoxyphenyl)-2-butanone
Dehydro-isolongifolene
N6,N6-dimethyllysine
FAHFA 36:2
SL 10:0;O/18:0
f
Hits 3 10 20
p.adjust
Glycerophospholipid metabolism
Biosynthesis of phenylpropanoids
Secondary bile acid biosynthesis
Alanine, aspartate and glutamate metabolism
Sphingolipid signaling pathway
Choline metabolism in cancer
Glycosylphosphatidylinositol (GPI)-anchor biosynthesis
Necroptosis
Fc epsilon RI signaling pathway
Neuroactive ligand-receptor interaction
Retrograde endocannabinoid signaling
D-Amino acid metabolism
Histidine metabolism
Glycine, serine and threonine metabolism
Cysteine and methionine metabolism
Rich factor
g
Control
Hypoxia
Hypoxia + Nit
Z-score
Glutamine (Gln)
Ornithine (Orn)
Proline (Pro)
Lysine (Lys)
Hydroxyproline (Hyp)
Asparagine (Asn)
Serine (Ser)
Glycine (Gly)
Histidine (His)
Leucine (Leu)
h
Serum Gln (μg/mL)
i
Serum Glu (μg/mL)
j
Serum Sar & Ala & BAla (μg/mL)
k
Serum Lys (μg/mL)
l
Serum Asn (μg/mL)
m
Serum Asp (μg/mL)
Control
Hypoxia
Hypoxia + Nit
n
Metagenome–Metabolome Association
L. murinus
L. reuteri
D. dubosii
Pa. intestinale
D. sp. C9
P. denticola
P. distasonis
K. pneumoniae
E. coli
P. merdae
|Spearman r|
Correlation
Pos. (p<0.05)
Pos. (ns)
Neg. (p<0.05)
Neg. (ns)
LPC O-18:1
1-Eicosanoyl-glycerol-3-P
14,19-Dihydro-aspidospermatine
FAHFA 36:2
Benzenebutanoic acid
Malonylcarnitine
Thr Ala Gln Glu
N6,N6-dimethyllysine
Isolongifolene (4,5,9,10-dehydro)
2-Arachidonyl glycerol ether
Oleanolic acid
5α-Androst-16-en-3α-ol
Calamenene
o
Pearson r = 0.95
Fecal Thr–Ala–Gln–Glu composite z-score
Prevotella denticola abundance
p
Pearson r = 0.52
Serum Gln (μg/mL)
Prevotella denticola abundance
q
Serum Gln (μg/mL)
r
Serum Sar & Ala & BAla (μg/mL)
s
Serum Asp (μg/mL)
Hypoxia
Hypoxia+P.d
Hypoxia+P.d+Nit

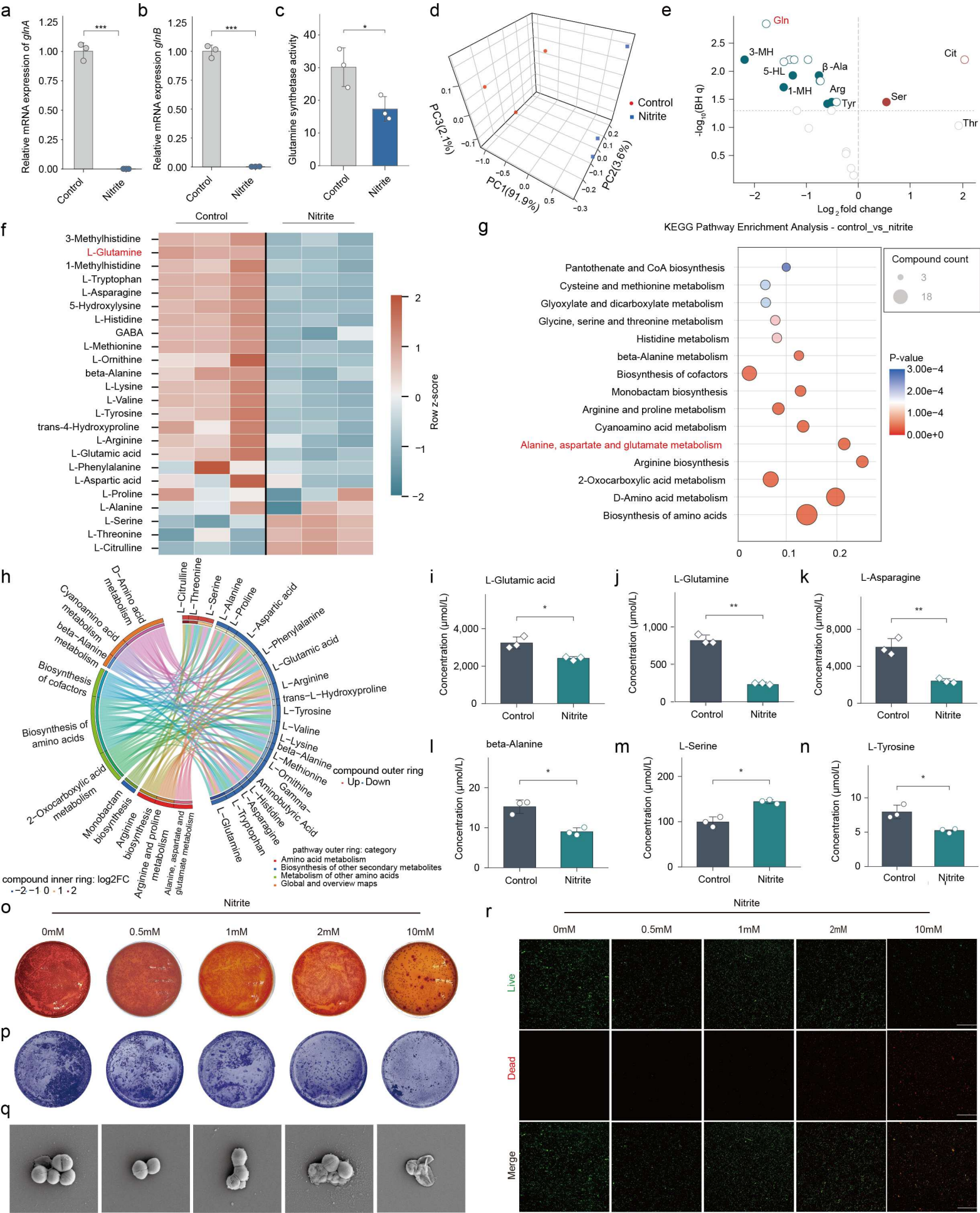
a
Relative mRNA expression of glnA
***
Control
Nitrite
b
Relative mRNA expression glnB
***
c
Glutamine synthetase activity
*
d
PC3(2.1%)
PC1(91.9%)
PC2(3.6%)
Control
Nitrite
e
Gln
3-MH
5-HL
1-MH
β-Ala
Arg
Tyr
Ser
Cit
Thr
-log10(BH q)
Log2 fold change
f
Control
Nitrite
3-Methylhistidine
L-Glutamine
1-Methylhistidine
L-Tryptophan
L-Asparagine
5-Hydroxylysine
L-Histidine
GABA
L-Methionine
L-Ornithine
beta-Alanine
L-Lysine
L-Valine
L-Tyrosine
trans-4-Hydroxyproline
L-Arginine
L-Glutamic acid
L-Phenylalanine
L-Aspartic acid
L-Proline
L-Alanine
L-Serine
L-Threonine
L-Citrulline
Row z-score
g
KEGG Pathway Enrichment Analysis - control_vs_nitrite
Pantothenate and CoA biosynthesis
Cysteine and methionine metabolism
Glyoxylate and dicarboxylate metabolism
Glycine, serine and threonine metabolism
Histidine metabolism
beta-Alanine metabolism
Biosynthesis of cofactors
Monobactam biosynthesis
Arginine and proline metabolism
Cyanoamino acid metabolism
Alanine, aspartate and glutamate metabolism
Arginine biosynthesis
2-Oxocarboxylic acid metabolism
D-Amino acid metabolism
Biosynthesis of amino acids
Compound count
P-value
h
compound outer ring
Up
Down
pathway outer ring: category
Amino acid metabolism
Biosynthesis of other secondary metabolites
Metabolism of other amino acids
Global and overview maps
compound inner ring: log2FC
i
L-Glutamic acid
Concentration (μmol/L)
j
L-Glutamine
k
L-Asparagine
l
beta-Alanine
m
L-Serine
n
L-Tyrosine
o
Nitrite
0mM
0.5mM
1mM
2mM
10mM
p
q
r
Nitrite
Live
Dead
Merge

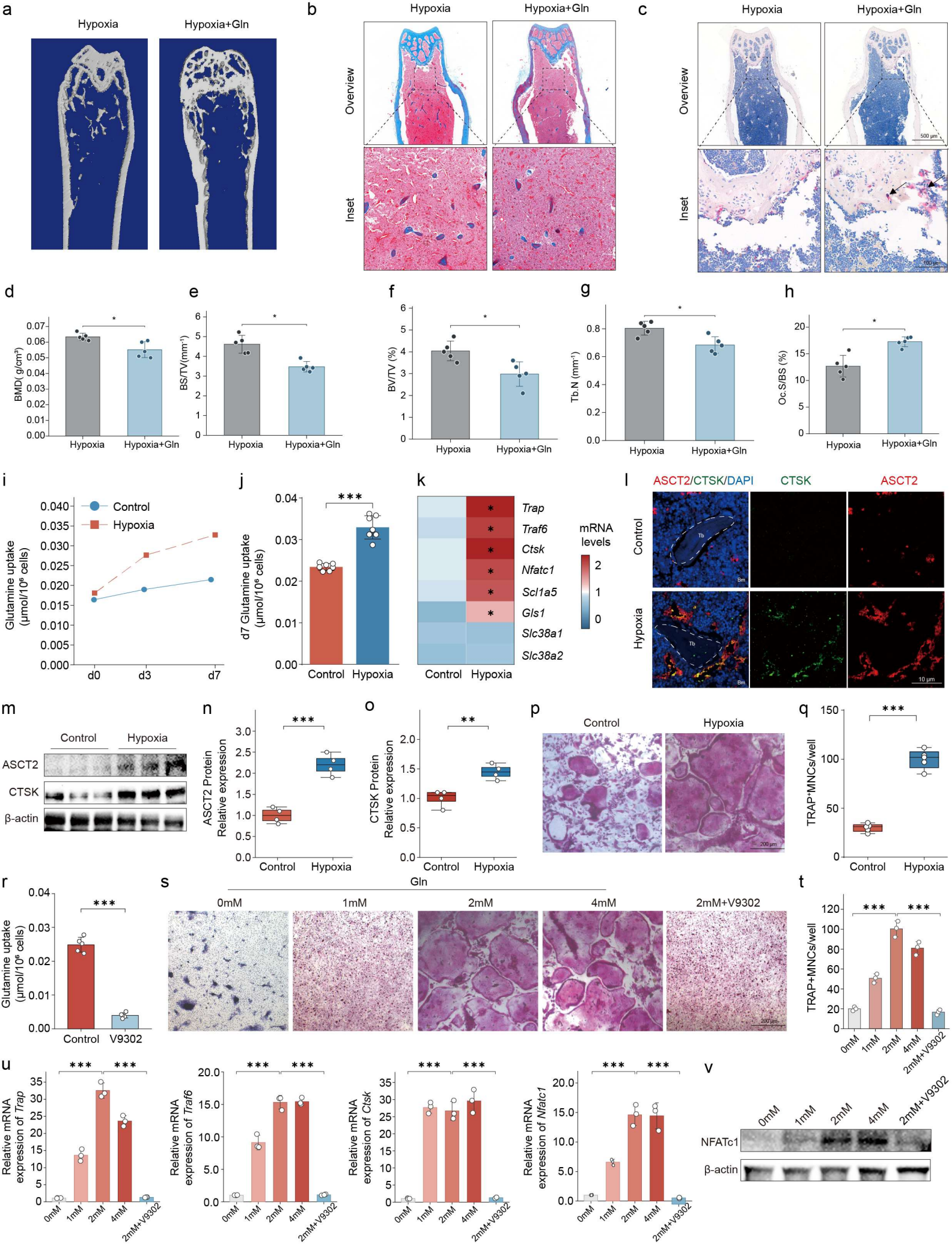
a
Hypoxia
Hypoxia+Gln
b
Hypoxia
Hypoxia+Gln
Overview
Inset
c
Hypoxia
Hypoxia+Gln
Overview
Inset
500 μm
100 μm
d
BMD(g/cm³)
Hypoxia
Hypoxia+Gln
e
BS/TV(mm⁻¹)
Hypoxia
Hypoxia+Gln
f
BV/TV (%)
Hypoxia
Hypoxia+Gln
g
Tb.N (mm⁻¹)
Hypoxia
Hypoxia+Gln
h
Oc.S/BS (%)
Hypoxia
Hypoxia+Gln
i
Control
Hypoxia
Glutamine uptake (μmol/10⁶ cells)
d0
d3
d7
j
d7 Glutamine uptake (μmol/10⁶ cells)
Control
Hypoxia
k
Trap
Traf6
Ctsk
Nfatc1
Scl1a5
Gls1
Slc38a1
Slc38a2
mRNA levels
Control
Hypoxia
l
ASCT2/CTSK/DAPI
CTSK
ASCT2
Control
Hypoxia
Tb
Bm
10 μm
m
Control
Hypoxia
ASCT2
CTSK
β-actin
n
ASCT2 Protein Relative expression
Control
Hypoxia
o
CTSK Protein Relative expression
Control
Hypoxia
p
Control
Hypoxia
200 μm
q
TRAP⁺MNCs/well
Control
Hypoxia
r
Glutamine uptake (μmol/10⁶ cells)
Control
V9302
s
Gln
0mM
1mM
2mM
4mM
2mM+V9302
200 μm
t
TRAP+MNCs/well
0mM
1mM
2mM
4mM
2mM+V9302
u
Relative mRNA expression of Trap
Relative mRNA expression of Traf6
Relative mRNA expression of Ctsk
Relative mRNA expression of Nfatc1
0mM
1mM
2mM
4mM
2mM+V9302
v
0mM
1mM
2mM
4mM
2mM+V9302
NFATc1
β-actin

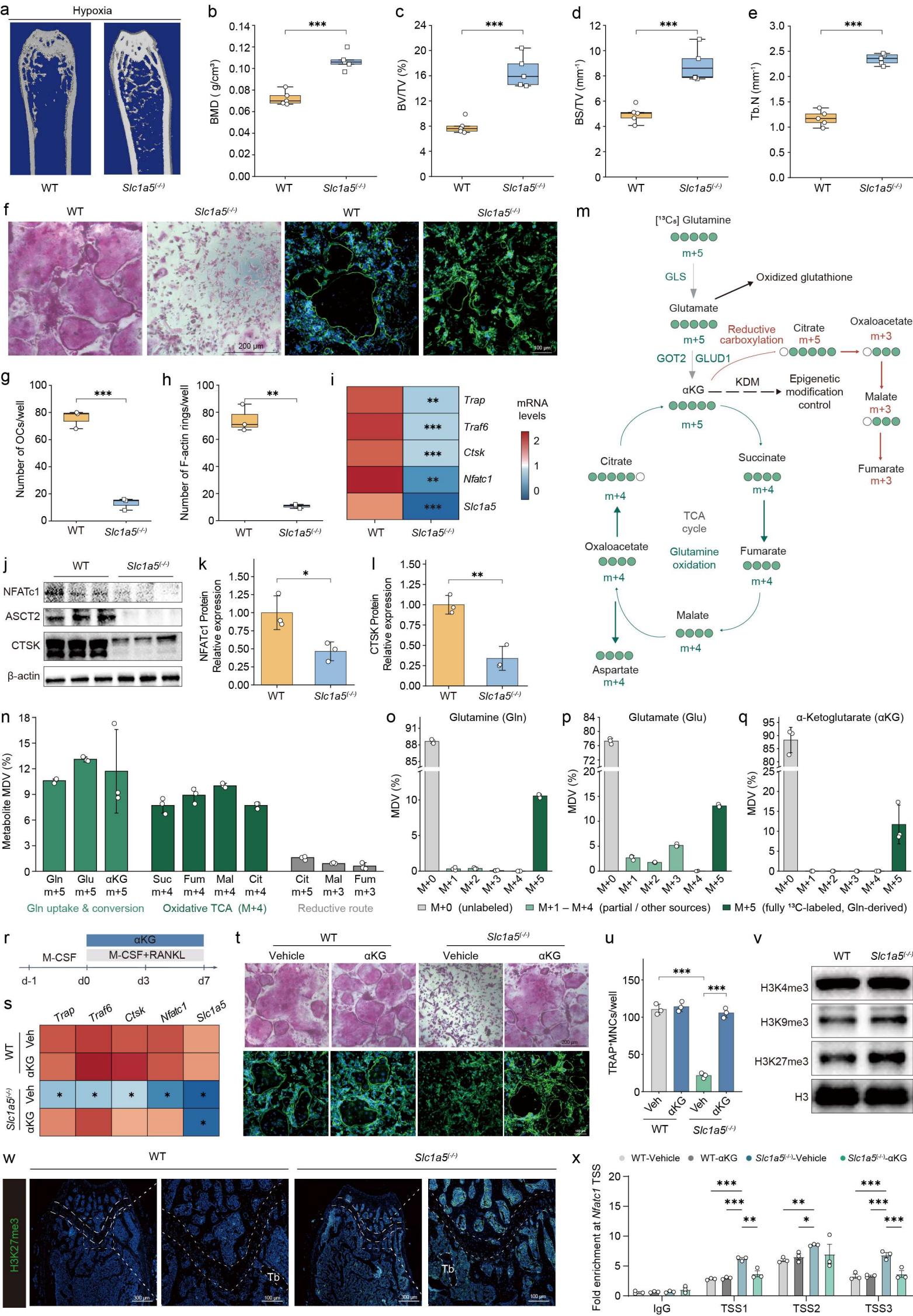
a
Hypoxia
WT
Slc1a5(-/-)
b
BMD (g/cm³)
c
BV/TV (%)
d
BS/TV (mm⁻¹)
e
Tb.N (mm⁻¹)
f
200 μm
100 μm
g
Number of OCs/well
h
Number of F-actin rings/well
i
Trap
Traf6
Ctsk
Nfatc1
Slc1a5
mRNA levels
j
NFATc1
ASCT2
CTSK
β-actin
k
NFATc1 Protein Relative expression
l
CTSK Protein Relative expression
m
[¹³C₅] Glutamine
m+5
GLS
Oxidized glutathione
Glutamate
Reductive carboxylation
Citrate
Oxaloacetate
m+3
GOT2
GLUD1
αKG
KDM
Epigenetic modification control
Malate
Fumarate
Succinate
m+4
TCA cycle
Glutamine oxidation
Aspartate
n
Metabolite MDV (%)
Gln m+5
Glu m+5
αKG m+5
Suc m+4
Fum m+4
Mal m+4
Cit m+4
Cit m+5
Mal m+3
Fum m+3
Gln uptake & conversion
Oxidative TCA (M+4)
Reductive route
o
Glutamine (Gln)
p
Glutamate (Glu)
q
α-Ketoglutarate (αKG)
MDV (%)
M+0
M+1
M+2
M+3
M+4
M+5
M+0 (unlabeled)
M+1 – M+4 (partial / other sources)
M+5 (fully ¹³C-labeled, Gln-derived)
r
αKG
M-CSF
M-CSF+RANKL
d-1
d0
d3
d7
s
Trap
Traf6
Ctsk
Nfatc1
Slc1a5
WT
Slc1a5(-/-)
Veh
αKG
t
WT
Slc1a5(-/-)
Vehicle
αKG
200 μm
u
TRAP⁺MNCs/well
v
H3K4me3
H3K9me3
H3K27me3
H3
w
H3K27me3
Tb
300 μm
100 μm
x
WT-Vehicle
WT-αKG
Slc1a5(-/-)-Vehicle
Slc1a5(-/-)-αKG
Fold enrichment at Nfatc1 TSS
IgG
TSS1
TSS2
TSS3

Supplementary Files

This is a list of supplementary files associated with this preprint. Click to download.

- SupplementaryInformation.docx
- F8.png